Observations and Analysis of the Horizontal Structure of a Tidal Jet at Deep Scour Holes

Broekema, Y. B.; Labeur, R. J.; Uijttewaal, W. S.J.

DOI
10.1029/2018JF004754

Publication date
2018

Document Version
Final published version

Published in
Journal of Geophysical Research: Earth Surface

Citation (APA)
Broekema, Y. B., Labeur, R. J., & Uijttewaal, W. S. J. (2018). Observations and Analysis of the Horizontal Structure of a Tidal Jet at Deep Scour Holes. *Journal of Geophysical Research: Earth Surface*, *123*(12), 3162-3189. https://doi.org/10.1029/2018JF004754

AGU100 ADVANCING EARTH AND SPACE SCIENCE

JGR

Journal of Geophysical Research: Earth Surface

RESEARCH ARTICLE

10.1029/2018JF004754

Observations and Analysis of the Horizontal Structure of a Tidal Jet at Deep Scour Holes

Y. B. Broekema[1], **R. J. Labeur**[1], **and W. S. J. Uijttewaal**[1]

[1]Department of Hydraulic Engineering, Delft University of Technology, Delft, Netherlands

Key Points:
- The tidal jet contracts toward the deepest part of the scour hole, maintaining high scour potential
- Vertical flow separation may be suppressed due to acceleration resulting from the horizontal contraction of the jet
- The horizontal structure of the jet is well explained by conservation of potential vorticity

Correspondence to:
Y. B. Broekema,
Y.B.Broekema@tudelft.nl

Citation:
Broekema, Y., Labeur, R. J., & Uijttewaal, W. (2018). Observations and analysis of the horizontal structure of a tidal jet at deep scour holes. *Journal of Geophysical Research: Earth Surface*, *123*, 3162–3189. https://doi.org/10.1029/2018JF004754

Received 11 MAY 2018
Accepted 6 NOV 2018
Accepted article online 12 NOV 2018
Published online 5 DEC 2018

Abstract Scour in the vicinity of a hydraulic structure may compromise its geotechnical stability or that of nearby structures. Much fundamental research has been dedicated to the understanding and prediction of these processes, in order to enable the efficient design of mitigation measures. While most of these efforts consider laterally uniform flows, nonuniformity is the rule rather than the exception. This study presents field observations near the storm surge barrier in the Eastern Scheldt estuary, The Netherlands, where significant scour holes have developed. The tidal flow through this semi-open barrier exhibits characteristics of a shallow jet. A pronounced contraction of this jet toward the nearby scour hole during particular stages of the tidal cycle is revealed, attributed to potential vorticity conservation; the depth-averaged vertical vorticity increases proportionally to the depth increase. Measurements show a vertically uniform velocity profile in the scour hole that is attributed to a reduction of the adverse pressure gradient due to the contraction, that suppresses boundary layer separation from the upstream slope of the scour hole. A positive feedback mechanism is thus revealed; lateral velocity gradients lead to relatively high near-bed velocities in the scour hole which enhances erosion—causing an even stronger horizontal contraction—maintaining the scouring potential. If the upstream flow field is laterally uniform (observed around slack tide), horizontal contraction does not occur, and the boundary layer separates from the upstream slope. The scour depth will then tend to an equilibrium. The results infer the importance of the nonuniformity of the horizontal flow field.

Plain Language Summary Large-scale erosion of an alluvial bed in the vicinity of hydraulic structures (scour) is a common problem, with potentially large consequences: the geotechnical stability of the structure may get compromised. A detailed understanding of the interaction between the hydrodynamics (flow) and the morphodynamics (response of the sandy bed) is crucial to accurately predict the scour process and subsequent mitigation strategies. In this study, we show that under certain conditions, the scour process may be self-amplifying. For a flow with large horizontal velocity differences, the scour hole may sustain (or increase) these velocity differences, leading to a concentrated flow in the deepest part of the scour hole. As a result, the scour potential remains high, whereas it would be expected that the scour potential decreases proportionally to the increase in scour depth. A good understanding of these conditions may help in assessing the vulnerability of hydraulic structures located in waterways like rivers, tidal channels, or estuaries and determine optimal strategies to mitigate potential risks from scour hole formation.

1. Introduction

Bridges, sluices, and storm surge barriers are typical examples of hydraulic structures situated in water systems like rivers, channels, and tidal inlets. These structures commonly reduce the local conveyance cross section leading to acceleration—and subsequent deceleration—of the flow passing the structure. In the presence of an alluvial bed, this may lead to large-scale erosion (scour) in the vicinity of the structure, with potentially large consequences for its structural integrity (Hoffmans & Pilarczyk, 1995). To prevent these problems, bed protection is often applied which should either reduce the scour depth or keep the scour at a safe distance from the structure. The design of such a bed protection is based on the maximum acceptable scour depth during the lifetime of the structure at a certain distance away from it, such that geotechnical instabilities that may result from the scouring process do not cause structural failure (Hoffmans & Pilarczyk, 1995). This requires fundamental understanding of the interaction between the (turbulent) water motion and the erodible bed in the vicinity of the structure (Bey et al., 2007; Dargahi, 2003; Hogg et al., 1997; Manes & Brocchini, 2015).

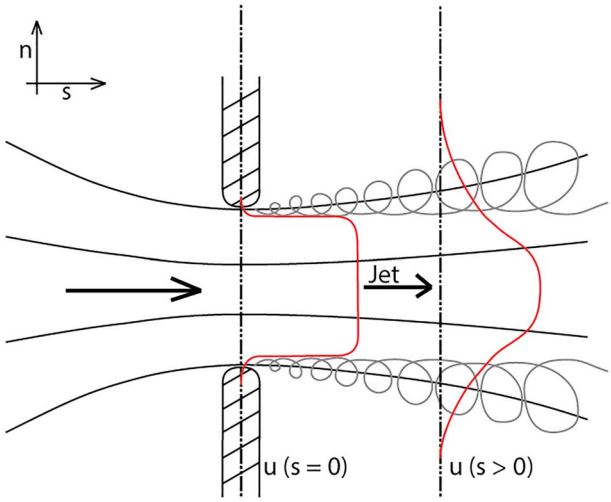

Figure 1. Top-view sketch of a shallow jet in the horizontal *sn* plane induced by a local cross-section reduction at a hydraulic structure. The hydraulic structure is located at $s = 0$, and downstream of the structure a free shear layer containing large vortical structures develops on either side of the jet, causing the flow to spread laterally for $s > 0$.

Traditionally, the temporal evolution of a scour hole has not been considered important for the final scour hole configuration (Termini & Sammartano, 2012). The majority of the studies investigating scour are therefore limited to the formulation of empirical equations allowing the estimation of the final maximum depth and length of the scour hole (Breusers et al., 1977; D'Agostino & Ferro, 2004; Lenzi et al., 2002). Generally, these formulations are (semi)empirical and only applicable on similar geometries as those investigated in the respective studies (Balachandar et al., 2000). Therefore, their application to different conditions may lead to inaccurate predictions of the scouring process. More advanced studies, which also consider the underlying flow and its turbulence characteristics, either neglect the temporal development of the scour hole (see Guan et al., 2014; Hoffmans & Booij, 1993) or neglect the scour occurring at larger downstream distances (see Dargahi, 1990; Melville, 1995; Rajkumar & Dey, 2008). Furthermore, fundamental research of scour hole formation is mainly performed in a 2D-vertical framework, as is also the case with the aforementioned studies. In reality, velocity differences in the horizontal plane can often not be neglected, as the surrounding bathymetry or the (partial) obstruction of the flow by the structure generally involves lateral velocity gradients. For a better understanding of scour hole formation, improved insight in the (three-dimensional) flow characteristics downstream of hydraulic structures is needed.

Due to the reduction of the conveyance cross section at a hydraulic structure, the flow downstream of it often has the characteristics of a jet. A free shear layer develops on either side of the jet, growing in downstream distance, causing the flow to spread laterally (Cohen, 2012). This process is schematized in Figure 1.

In rivers or channels without tidal influence, this jet is quasi-steady, that is, there is no temporal variation of the mean velocity structure. In the free shear layer, lateral velocity differences generate large horizontal vortices (Dracos et al., 1992; Jirka, 2001) that redistribute horizontal momentum (Talstra, 2011; van Prooijen & Uijttewaal, 2002). These coherent structures are usually associated with regions of high turbulence intensity (Babarutsi et al., 1989).

At tidal inlets, the situation can be quite different. The ambient flow often contracts, even in absence of hydraulic structures, due to the local geometry of the coastline. Furthermore, the tidal jets vary periodically in time in response to the tide, and a significant asymmetry between ebb and flood flow may exist (Valle-Levinson & Guo, 2009). Developing jets are typically associated with a vortex cap of two counter rotating vortices (Bryant et al., 2012; Hench et al., 2002; Wolanski et al., 1988). They form and grow directly downstream of the tidal inlet (Nicolau Del Roure et al., 2009) due to the growing intensity of the shear layer that occurs after slack tide (Wells & van Heijst, 2003). Another mechanism that may generate these large-scale vortices is flow separation from the nearshore boundary layer and subsequent roll up of shear instabilities (Signell & Geyer, 1991).

Although the influence of lateral variation of the bed topography on the structure and development of jets and mixing layers has been studied extensively (Besio et al., 2012; Stocchino et al., 2011; van Prooijen et al., 2005; Wan et al., 2015), knowledge on the influence of longitudinal topographical variability on the structure of jets and mixing layers is limited. At a location where the flow depth increases, as in a scour hole, the influence of the bed friction will decrease. For a steady flow with a uniform slope of the free surface, this may result in a higher velocity through the deeper part of the domain, generating additional lateral shear (Shiono & Knight, 1991). However, for this effect to be significant, a relatively large length scale for adaptation of the flow to the change of bed friction of approximately 200 times the water depth is needed, which is generally much larger than the horizontal dimensions of the scour hole. More relevant in this respect is the situation that may occur in sharp river bends with local deep scour holes. The increase in cross-sectional area associated with the scour hole may cause lateral flow separation (Blanckaert, 2010; Schnauder & Sukhodolov, 2012). The resulting horizontal recirculation involves jet-like structures of the flow (Vermeulen et al., 2015). An important mechanism in the development of flows with large horizontal gradients is potential vorticity conservation, as a result of which variable bed topography will influence the background vorticity field by vertical stretching and horizontal contraction of vortex tubes (Poulin & Flierl, 2005). Furthermore, Brocchini (2013) has shown that bed discontinuities may form an important source of potential vorticity generation.

In this study the flow pattern downstream of a storm surge barrier in a tidal inlet in the Netherlands (the Eastern Scheldt Storm Surge Barrier [ES-SSB]) will be investigated, using data from field measurements. At this storm surge barrier a bed protection is applied on both sides of the construction, which extends 550 to 650 m from the barrier. Downstream of the applied bed protection, large scour holes have developed (van Velzen et al., 2015). A computation using 2D-vertical formulations for the case of scour behind a sill with bed protection (Hoffmans & Verheij, 1997) shows that the expected equilibrium scour depth at the storm surge barrier is approximately 2.2 times the original water depth. The current scour depth observed at the barrier is around 2.2 times the original water depth, so indeed according to theory, equilibrium should have been reached. However, continuous monitoring of the situation has revealed that erosion is still ongoing, indicating that a 2D-vertical approximation is lacking a part of the phenomenology.

We will investigate the relation between the complex bed topography and the flow structure at the scour holes through an analysis of flow data and mathematical modeling of a schematized geometry. It will be inferred that the horizontal nonuniformity of the flow is crucial in explaining the ongoing development of the scour.

2. Data Acquisition

2.1. Study Area

The Eastern Scheldt is a tidal basin in the southwestern part of the Netherlands that was partly closed by a storm surge barrier in response to a large flooding event in 1953. The ES-SSB is one of the primary flood defense structures to protect the southern part of The Netherlands against extreme high-water levels. It is 9 km long and has a semi-open structure, consisting partly of dams and partly of gates to maintain a tidal saline-water habitat in the Eastern Scheldt estuary. The dams cover 5 km of the entrance, the remaining 4 km are covered by the three main inlets to the estuary, from south to north: *Roompot*, *Schaar*, and *Hammen* (see Figure 2a). The inlets consist of 31, 15, and 16 gates, respectively, each with a width of 39.5 m. The sills in the inlet are constructed in such a way that they follow the profile of the former tidal channels (van Velzen et al., 2015), such that the water depth above the sills decreases from the center of the inlet outward. On average, the water depth on top of the sills is approximately 10 m, while downstream of the sills, on top of the bed protection, the water depth is 20–25 m. The inlets are approximately 1,000–1,500 m wide. The tidal range near the ES-SSB is about 2.5 m, and characteristic maximum depth-averaged velocities on top of the bed protection are in the order of 1.5–2 m/s.

On each side of the ES-SSB, a bed protection consisting of rock material is applied over a distance of 550 to 650 m from the barrier to safeguard its stability. Continuous monitoring of the bathymetry since the construction of the barrier in 1986 has shown that on both sides of the barrier, downstream of the applied bed protection, large scour holes have developed (van Velzen et al., 2015). Half-yearly monitoring studies using a multibeam echosounder show that locally water depths of up to 60 m occur, associated with roughly 40 m of scour. The bathymetry of the Eastern Scheldt in the vicinity of the storm surge barrier is shown in Figure 2b, where d denotes the water depth w.r.t. mean sea level and X and Y are coordinates according to the Dutch national RijksDriehoek-coordinate system (Schreutelkamp & Strang van Hees, 2001).

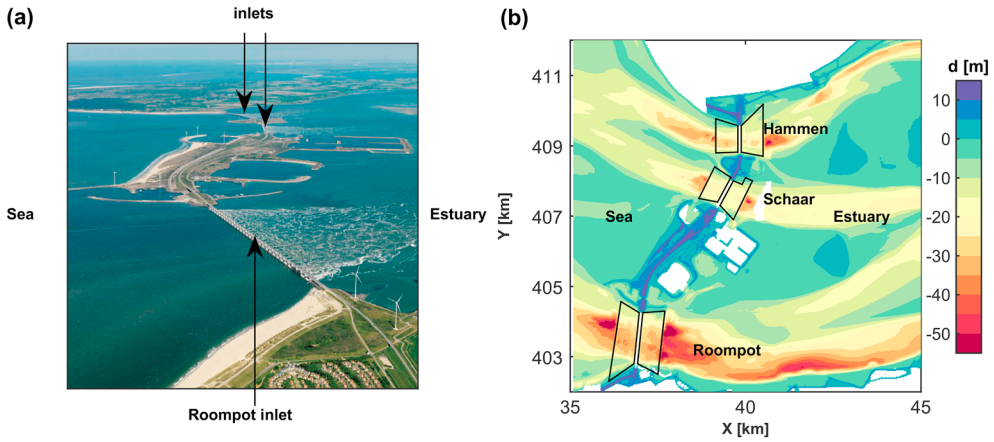

Figure 2. Aerial photograph of the Eastern Scheldt storm surge barrier showing from bottom (S) to top (N): Roompot inlet, Neeltje Jans construction island, Schaar inlet, Roggeplaat construction island, and Hammen inlet (a); bed topography in the near area of the storm surge barrier (January 2013) showing the impermeable part of the barrier (dark blue strip) and the scour holes (red areas) (b). The location of the bed protection at each inlet is roughly given by the solid black lines.

The area of study concerns the scour holes and the adjacent bed protection at the estuary side of the barrier in the Roompot and Schaar inlets, respectively, close to the ES-SSB.

2.2. Aerial Photographs

To investigate the horizontal structure of the flow field passing the barrier, aerial photographs are used that are publicly available through Rijkswaterstaat, the Dutch ministry of public works. Additionally, satellite images of the region, showing characteristic features of the surface flow, are available through Google Earth. Flow separation occurring at the openings of the ES-SSB causes large turbulent structures on top of the base flow. These coherent structures, often visible through floating foam, can be observed from satellites which provides a qualitative impression of the large-scale, horizontal flow patterns in the wake of the barrier.

2.3. Flow Velocity Data

An extensive field campaign was conducted between January 2014 and July 2016, measuring flow velocities in the vicinity of the scour holes. At each of the three inlets, flow velocities were measured using Acoustic Doppler Current Profiler (ADCP) sensors (Teledyne RDI Workhorse Sentinel) mounted on a vessel sailing along specific transects.

The data that are used in this paper were collected at the Roompot inlet (on 22 June 2016) and at the Schaar inlet (on 19 January 2015) along a number of transects, shown in Figures 3a and 3b, respectively. At both inlets three types of transect are distinguished:

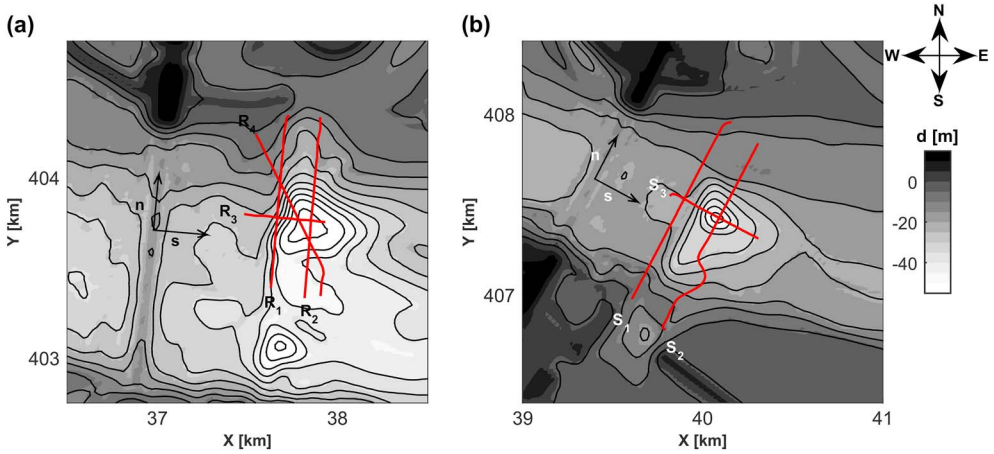

Figure 3. Sailed Acoustic Doppler Current Profiler transects at the Roompot inlet on 22 June 2016 (a) and Schaar inlet on 19 January 2015 (b). Gray scale indicates the bed level with respect to mean sea level of January 2013. Local (*s*, *n*) coordinate system used for flow analysis is plotted at the location of the barrier for both inlets.

1. transects parallel to the barrier right above the bed protection,
2. transects parallel to the barrier through the deepest part of the scour hole, and
3. transects through the deepest part of the scour hole perpendicular to the barrier.

These transects are denoted with, respectively, R_1, R_2, and R_3, for the Roompot inlet and S_1, S_2, and S_3 for the Schaar inlet, as shown in Figure 3. At the eastern side of the Roompot inlet, an additional transect (R_4) was sailed to obtain higher resolution of the data in the recirculation zone (see section 3). Transect S_2 is curved, because the observation vessel had to sail around a safety buoy. For the same reason, transect R_4 deviates from a straight line as well. Data were collected during one flood period, during which the layout of transects was sailed repetitively. The sailing speed was approximately 4 m/s, for which completing the transect layout at the Roompot inlet required half an hour of sailing time, whereas the completion of the transect layout at the Schaar inlet took 25 min. As such, at the Roompot inlet, we have a total of 14 cycles of the transects and 17 cycles at the Schaar inlet. The transects plotted in Figure 3 are the actually sailed transects during the first cycle. Subsequent transects may deviate slightly from the intended tracks, especially when the currents became stronger.

The ADCP sensors collected data using a broadband signal with a frequency of 614 kHz and a depth cell size of 1 m. The beam angle of the instrument was 20° with respect to the vertical, and the standard deviation per transmitted pulse (ping) was equal to 7.0 cm/s. The ensemble time was approximately 4.5 s, and (only) one ping was used per ensemble.

2.4. Flow Data Processing

In the data analysis, we use a global coordinate system, which is the Dutch National RijksDriehoek-coordinate system (X, Y), and a local (s, n, z) coordinate system. In the local coordinate system, the s axis aligns with the streamwise direction of the tidal channels at the ES-SSB, the n axis is perpendicular to the s axis and runs parallel to the barrier, and the z axis is the vertical axis (see Figure 3). All flow data analyses are performed in the local coordinate system for convenience in the modeling stage of the study. The global X, Y-coordinate system is used for plotting bathymetric data and for georeferencing the flow data. The ADCP data are used to determine the large-scale characteristics of the horizontal flow field and to determine the vertical structure of the flow along a transect through the scour hole. For investigating the horizontal flow structure, the observed velocities are averaged over the depth, component wise, yielding a number of data points in s, n, t space. Next, a spatiotemporal grid with horizontal grid sizes $\Delta s = 30$ m, $\Delta n = 30$ m, and time steps $\Delta T = 10$ min containing all these data points is used to interpolate the data. Velocities were interpolated to the nodal points of the grid using simple linear interpolation. Since not the entire water column was sampled, velocities were assumed zero at the bed and linearly interpolated up until the first data point. Additionally, the velocity at the surface was assumed to have the same value as the first measurement point below the surface. Alternatively, we simply averaged the velocities over part of the water column that was measured. Comparing these two methods showed that the results were not sensitive to the method, probably because of the relatively large water depths. As such, the large-scale motion of the water did not change significantly when using a different averaging method. The ADCP data are used to determine the vertical structure of the flow along a transect through the scour hole. To this end, the velocity measured by the ADCP is decomposed along the s, z axis along transect R_3 at the Roompot inlet. The obtained velocity profile along the transect is the instantaneous velocity (turbulence is not averaged out), since only one ping per ensemble was used. To obtain a valid mean velocity, we have applied a moving average filter along the transect, where each vertical profile on the transect was averaged with the previous and the following profile. Vertical profiles are then averaged over three ensembles, which is likely not sufficient to really average out the turbulence. However, Buschman (2017) has compared the velocity data collected by boat to data obtained with ADCP's that were anchored on the bed and found that averaging over three ensembles provides a vertical profile of the velocity that is generally comparable to that of the bed-mounted ADCP. The depth-averaged velocities are, however, less sensitive to this issue due to the depth averaging.

From the interpolated depth-averaged velocity data, the depth-averaged vertical vorticity $\bar{\omega}_z$ was computed, defined by

$$\bar{\omega}_z = \frac{\partial \bar{u}_n}{\partial s} - \frac{\partial \bar{u}_s}{\partial n}, \tag{1}$$

where $\bar{u}_s$ and $\bar{u}_n$ are the depth-averaged velocity components in the (longitudinal) s direction and (lateral) n direction, respectively. Gradients in equation (1) were computed using central differences. Since the vertical

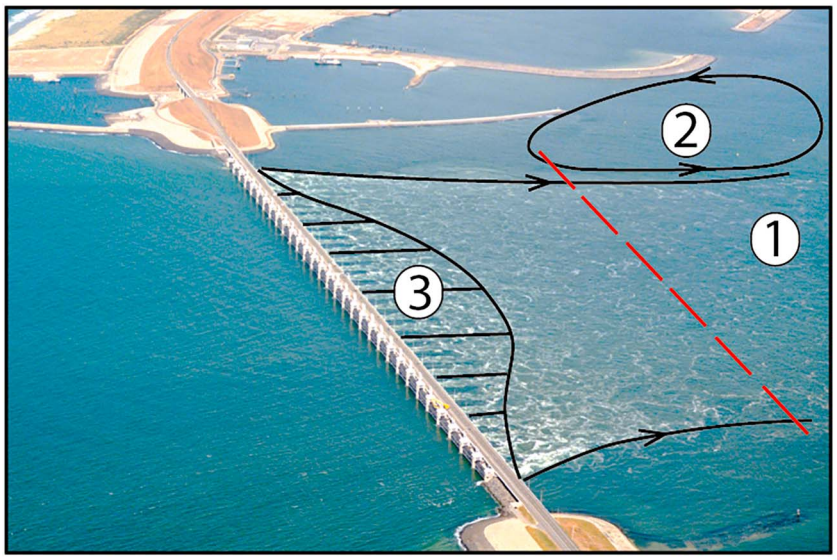

Figure 4. Aerial photograph of the flow at the Roompot inlet of the Eastern Scheldt Storm Surge Barrier during flood, looking to the Northeast, red-dotted line denotes the edge of the bed protection; upon passing the barrier, the flow is strongly contracting, and maximum contraction is found at the deepest part of the scour (1); the absence of foam in the region adjacent to the mainflow indicates that a recirculating motion is present (2); the outflow from the barrier is schematized as a jet (3). Source: https://beeldbank.rws.nl, Rijkswaterstaat.

vorticity computed from the depth-averaged velocity is the only component of the vorticity that we consider in this study, we adopt the notation $\bar{\omega}_z = \omega$.

3. Data Analysis

This section presents the field data collected at the ES-SSB. We will first assess, using aerial photos, the expected flow patterns in the near vicinity of the barrier. Subsequently, we will analyze the horizontal flow structure by showing velocity and vorticity data at the scour hole obtained from the ADCP's. Next, the vertical structure of the flow through the deepest part of the scour will be investigated.

3.1. Characteristic Flow Features

An aerial photograph of the ES-SSB is shown in Figure 4 (the camera is looking toward the Roompot inlet from the Southwest), with the flow entering the Eastern Scheldt basin (flood). The location of the edge of the bed protection is indicated by the red-dotted line. Downstream of the barrier, the flow is contracting horizontally with the maximum contraction found at the location of deepest scour (1). The absence of foam to the left of this location indicates that a recirculation zone is present adjacent to the main flow (2). The natural local topography at the barrier has a maximum water depth at the center of the channel, which is decreasing toward the sides. The barrier is constructed such that the sills follow this natural channel profile. Due to these local depth differences, it is expected that the horizontal velocity profile can be approximated as a shallow jet (3). The aerial photograph shows that in the center of the domain, the length of the wakes directly downstream of the piers is the largest, indicating that velocity is indeed highest in the center of the domain. This statement is further supported by model results from van Velzen et al. (2015). This will be discussed in more detail in section 4.

3.2. Depth-Averaged Flow Velocity

3.2.1. Roompot Inlet

Interpolated depth-averaged velocity fields at the Roompot inlet (22 June 2016) are plotted in Figure 5 for three different stages of the tidal cycle: about 1.5 hr after slack tide (T_1, Figures 5a and 5b), at maximum flood (T_2, Figures 5c and 5d), and 1 hr after maximum flood (T_3, Figures 5e and 5f). Both streamlines (left panels) and velocity magnitudes (right panels) are plotted. As a reference, the corresponding transects, $R_1 - R_4$, are included in the plot as red lines. Due to the local blockage by the barrier, there is a water level difference between the estuary side and the seaside of the barrier. This water level difference amounts to 26 cm at T_1, 78 cm at T_2, and 32 cm at T_3. The interpolated velocities may extend out of the convex hull of the theoretical

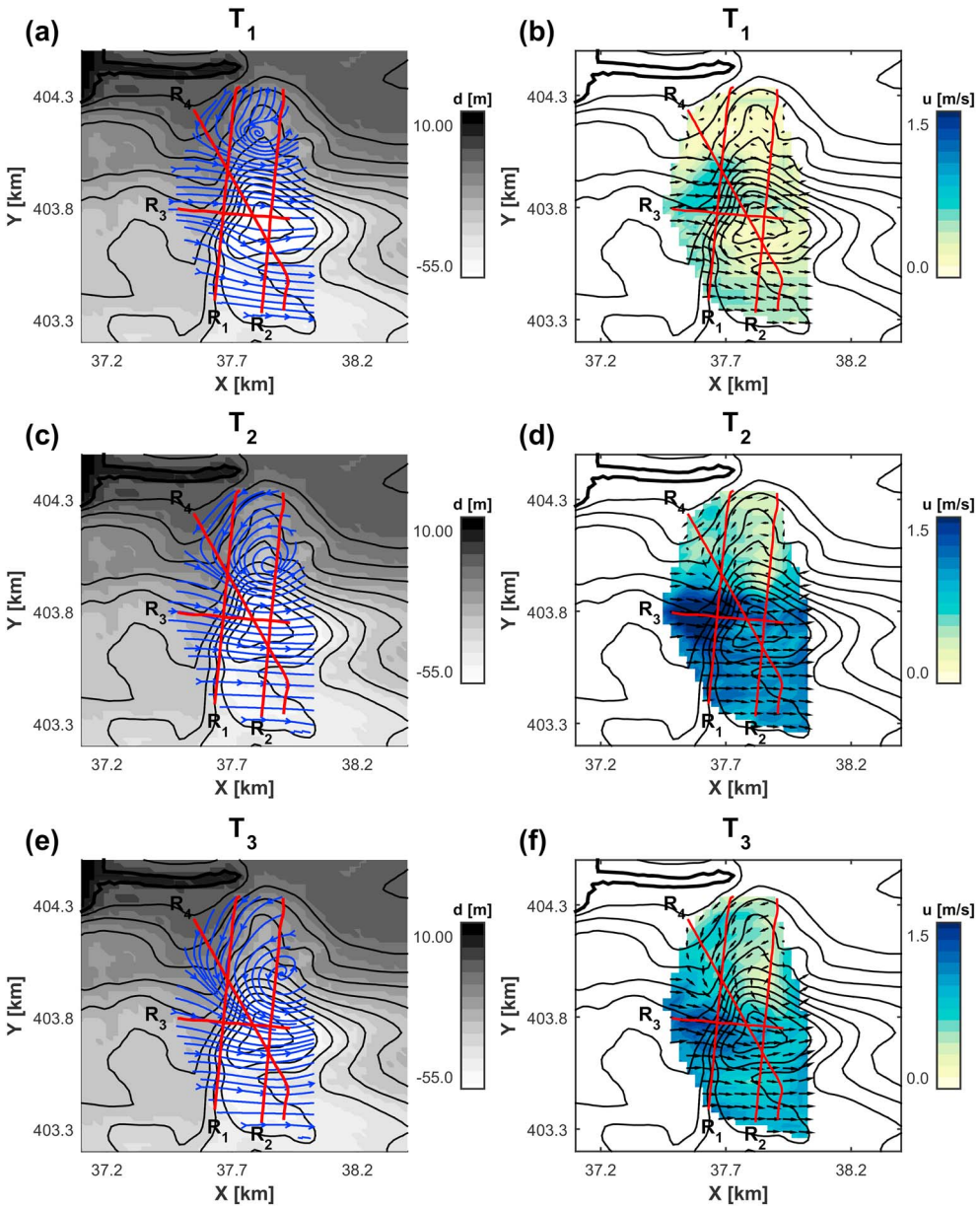

Figure 5. Interpolated depth-averaged flow field; streamlines (left panels) and velocity magnitude (right panels) at the Roompot inlet for three different stages of the tidal cycle: 1.5 hr after slack tide (a and b), at maximum flood (c and d), and 1 hr after maximum flood (e and f). As a reference, the sailed transects $R_1 - R_4$ are plotted in red. The gray scale in the left panels denotes the water depth and the color map in the right panels the velocity magnitude.

tracks plotted in Figure 3, which is explained by slight deviations of the actual sailed tracks from the theoretical tracks $R_1 - R_4$.

In Table 1, the cross-sectionally averaged streamwise flow velocity along a transect u_a, the difference in streamwise velocity along a transect Δu, and the relative velocity difference $\Delta u/u_a$ are given for transects R_1 and R_2 for the three different stages in the tidal cycle $T_1 - T_3$. The lateral velocity difference Δu is determined as the difference between the minimum and maximum velocities along these transects. Additionally, the water level difference Δh at each stage in the tidal cycle is given.

At time T_1 (Figures 5a and 5b), the flow is relatively uniform in lateral direction. A recirculation zone starts to develop at the northern side of the domain. Above the scour hole (and also to the south of the scour hole), horizontal streamlines are approximately straight. A slightly stronger flow is observed above the scour hole.

Table 1
Observed Values of Cross-Sectionally Averaged Streamwise Velocity u_a, Lateral Difference in Streamwise Velocity Over the Cross-Section Δu, and the Relative Lateral Velocity Difference, $\Delta u/u_a$, Along Transects R_1 and R_2 at the Roompot Inlet; Δh Is the Observed Water Level Difference Between the Inside and Outside of the Barrier

	Transect	u_a (m/s)	Δu (m/s)	$\frac{\Delta u}{u_a}$ (–)	Δh (m)
T_1: 1.5 hr after slack	R_1	0.33	0.67	2.03	0.26
	R_2	0.25	0.46	1.84	
T_2: maximum flood	R_1	0.66	1.66	2.50	0.78
	R_2	0.49	1.45	2.96	
T_3: 1 hr after maximum flood	R_1	0.44	1.40	3.18	0.32
	R_2	0.33	1.30	3.94	

This is likely a direct result of inlet topography at the barrier, which leads to a higher flow velocity in the center of the domain. Above the scour hole, both the cross-sectionally averaged flow velocity (u_a) and the velocity difference (Δu) are lower than above the bed protection (Table 1).

At time T_2 (Figures 5c and 5d), the recirculation zone in the north is much more pronounced than at time T_1. Large velocity differences in lateral direction are observed, and streamlines are converging toward the deepest part of the scour hole. As a result, the velocity in front of (and slightly above) the scour hole is significantly larger than the observed velocities elsewhere in the interpolated domain, and lateral velocity differences above the scour hole remain relatively large (Table 1). The average flow velocity decreases in the direction from R_1 to R_2, but the relative horizontal velocity difference ($\Delta u/u_a$) increases.

At time T_3 (Figures 5e and 5f), the horizontal extent of the recirculation zone has increased compared to time T_2. Lateral velocity differences are still clearly present, and streamlines are strongly converging toward the deepest part of the scour hole, resulting in an increase in relative horizontal velocity difference (Table 1). Although less apparent than during maximum flood, the flow velocity in front of and above the scour hole is still larger than elsewhere in the domain.

The magnitude of the streamwise velocity is correlated with the water level difference between the inside and outside of the barrier, as can be seen in both Table 1 and Figure 5. When this difference is larger, velocities are generally larger. However, the water level difference at T_1 is more or less equal to the water level difference at T_3 (26 and 32 cm, respectively), while the velocity at T_3 is significantly larger. The velocity difference between T_1 and T_3 for a similar water level difference is possibly related to inertial effects. Additionally, at time T_3, the conveyance cross section is reduced compared to T_1 due to the contracting nature of the flow and the relatively large horizontal extent of the recirculation zone.

3.2.2. Schaar Inlet

The interpolated depth-averaged velocity fields at the Schaar inlet (19 January 2015) are visualized in the same manner as the Roompot inlet, for the same three stages in the tidal cycle $T_1 - T_3$.

Table 2 lists u_a, Δu, and $\Delta u/u_a$ for transects S_1 and S_2 for times $T_1 - T_3$. Before discussing the observations at the Schaar inlet, we first show similarities and differences between the Schaar and Roompot inlet. First, the

Table 2
Observed Values of Cross-Sectionally Averaged Streamwise Velocity u_a, Difference in Streamwise Velocity Over the Cross-Section Δu and the Relative Velocity Difference $\Delta u/u_a$, Along Transects S_1 and S_2 at the Schaar Inlet

	Transect	u_a (m/s)	Δu (m/s)	$\frac{\Delta u}{u_a}$ (–)
T_1: 1.5 hr after slack	S_1	0.26	0.55	2.12
	S_2	0.22	0.42	1.83
T_2: maximum flood	S_1	0.46	1.39	3.00
	S_2	0.31	1.37	4.42
T_3: 1 hr after maximum flood	S_1	0.36	1.04	2.89
	S_2	0.20	1.15	5.75

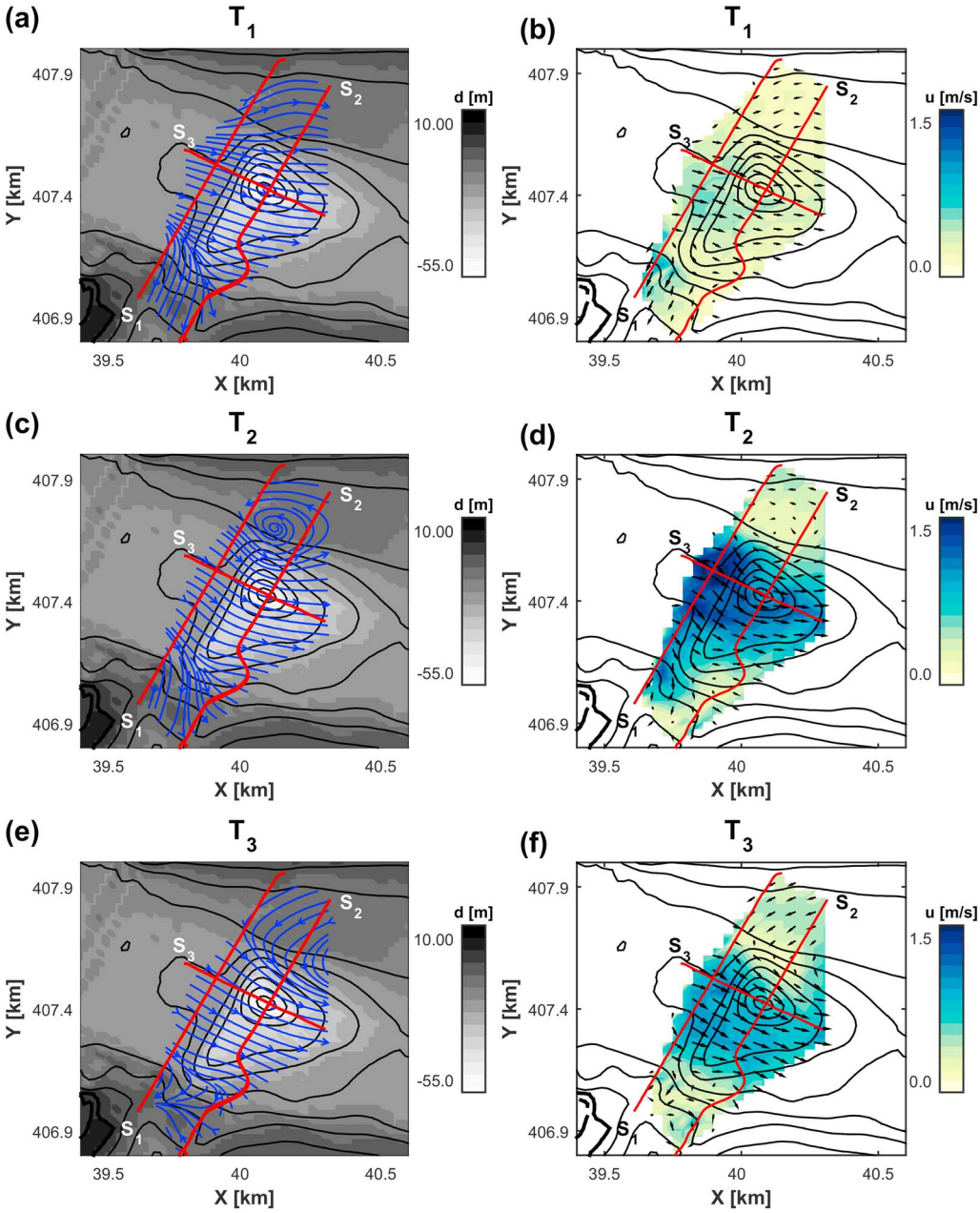

Figure 6. Interpolated depth-averaged flow field; streamlines (left panels) and velocity magnitude (right panels) at the Schaar inlet for three different stages of the tidal cycle: 1.5 hr after slack tide (a and b), at maximum flood (c and d), and 1 hr after maximum flood (e and f). As a reference, the sailed transects S_1 – S_3 are plotted in red. The gray scale in the left panels denotes the water depth and the color map in the right panels the velocity magnitude.

bathymetric data show that the seabed slope above the bed protection, where the jet develops, is approximately 1 in 50 for both the Roompot and the Schaar inlet. At the Schaar inlet, there is no tidal station at the seaside of the barrier, so the exact water level difference between the seaside and basin side of the barrier is unknown, although it is expected to be of the same order of magnitude as in the Roompot inlet. A difference between the Roompot inlet and the Schaar inlet is that at the Schaar inlet, on both sides of the barrier, there is a harbor in the Southern side of the domain in open connection with the sea. Furthermore, at the Roompot inlet, at the North side, a breakwater is present in front of the harbor entrance. At the Schaar inlet, there is a breakwater on the North side of the inlet as well, it is smaller and relatively located further away from the barrier axis. These geometrical details may locally influence the development of the flow.

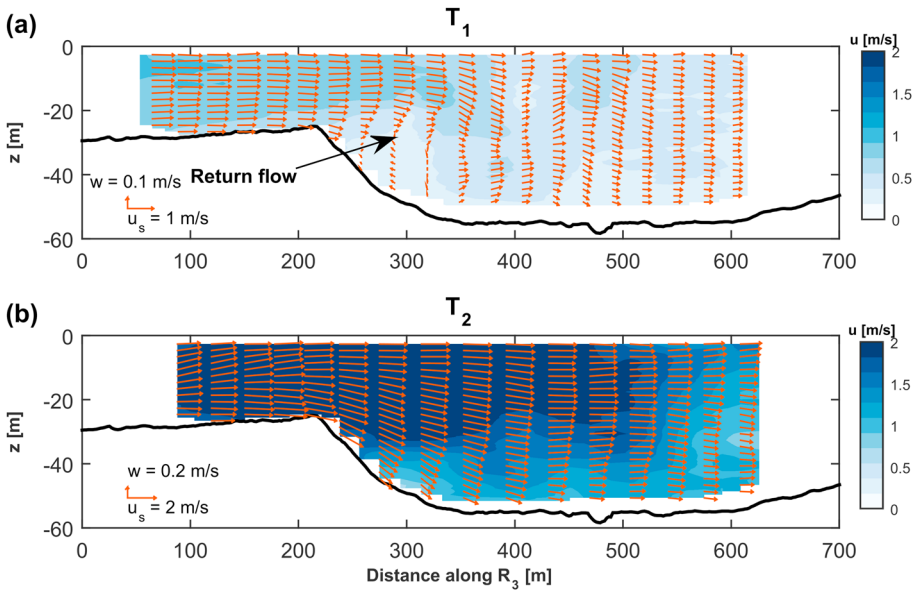

Figure 7. Flow in the s, z plane along transect R_3 at the Roompot inlet at time T_1 (a) and T_2 (b). The color map denotes the velocity magnitude.

At time T_1 (Figures 6a and 6b), the flow velocity is nearly uniform in lateral direction. Velocities are slightly higher at the deeper parts of the domain, similar to the observed flow in the Roompot inlet. However, streamlines are horizontally diverging. This is slightly different from what was observed at the Roompot inlet, which may be partially explained by the larger breakwater present in the North side of the Roompot inlet. The cross-sectionally averaged flow velocity and the lateral velocity difference are both decreasing from the bed protection toward the scour hole (Table 2). At the northern side of the domain, a recirculation zone starts to develop. At the southern side of the domain, water appears to be flowing toward the harbor inlet.

At time T_2 (Figures 6c and 6d), the recirculation zone in the north is well established. Similarly to the Roompot inlet, large lateral velocity differences are observed, and streamlines are converging toward the scour hole. The lateral velocity differences over the cross section remain high, while the average flow velocity decreases above the scour hole (Table 2). The convergence of the streamlines toward the scour hole appears to be less pronounced as that observed at the Roompot inlet at the same time instant.

The flow structure 1 hr after maximum flood (Figures 6e and 6f) is again similar to the flow structure at the Roompot inlet. Large lateral velocity differences persist (and even increase toward the scour hole), and the horizontal extent of the recirculation zone has become larger.

By comparing Figures 5 and 6, it appears that the structure of the flow as well as the flow velocities at both inlets are very similar, showing only minor differences. These are attributed to the smaller width of the Schaar inlet compared to the Roompot inlet but also to the presence of the harbor in the southern part of the Schaar inlet that draws a considerable part of the flow.

3.3. Vertical Velocity Component

In Figure 7, a vertical transect of the flow along cross-section R_3 at the Roompot inlet is plotted for two different stages of the tidal cycle: 1.5 hr after slack tide (T_1, Figure 7a) and maximum flood (T_2, Figure 7b).

At time T_1, return currents at the upstream side of the scour hole are clearly visible in the data (Figure 7a), indicating the occurrence of vertical flow separation. At time T_2, when the velocities are much higher, no return currents are observed, and the flow remains attached to the bed. High, downward vertical velocities of up to 20 cm/s are observed, advecting high momentum fluid to the deepest parts of the scour hole.

At time T_2, the vertical structure of the flow is significantly different from that at time T_1 and far more uniform than what would be expected considering the relatively steep slopes at the upstream end of the scour hole (Kwoll et al., 2016). At T_1, the depth-averaged streamwise flow velocity along the transect reduces proportionally to the streamwise increase in water depth, with an approximately 50% reduction of flow velocity from the

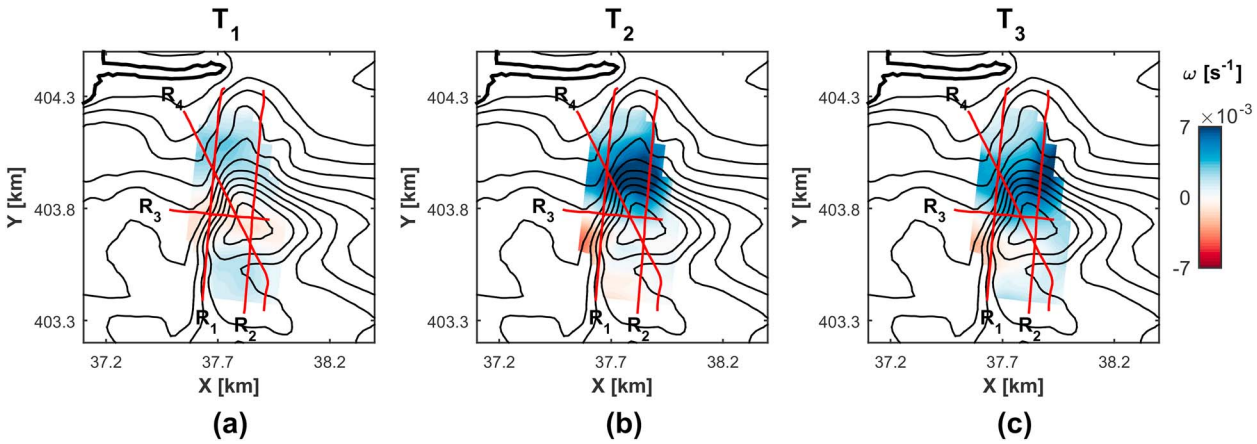

Figure 8. Vertical vorticity derived from the interpolated depth-averaged flow field at the Roompot inlet for three stages in the tidal cycle: 1.5 hr after slack tide (a), at maximum flood (b), and 1 hr after maximum flood (c). As a reference, boat transects R_1 –R_4 are plotted in red.

edge of the bed protection until the downstream end of the scour hole. At this stage of the tidal cycle there is limited lateral variability in the approaching flow upstream of the scour hole. The observed features of the vertical structure of the flow at T_1 show strong similarities with laboratory observations of flow in a 2D-vertical scour hole (e.g., Guan et al., 2014; Hoffmans & Booij, 1993).

At T_2, the situation is different. The reduction in depth-averaged streamwise flow velocity along the transect is less, which can be understood by considering the horizontally contracting nature of the flow at T_2. When large lateral velocity differences are present in the approaching flow upstream of the scour hole, a convergence of streamlines toward the deepest part of the scour hole and an increase in relative horizontal velocity difference were observed. These observations suggest that there is a link between the horizontal structure and the vertical structure of the flow, where the presence of lateral nonuniformities in the velocity distribution may counteract vertical flow separation.

The vertical flow phenomena observed at the Schaar inlet are essentially similar to the corresponding observed flow phenomena at the Roompot inlet. However, it was decided not to show the data from the Schaar inlet, as there were some gaps in the data due to malfunctioning of the ADCP, whereas there were none in the data at the Roompot inlet.

3.4. Depth-Averaged Vertical Vorticity

Figure 8 shows the vertical vorticity component as computed from the interpolated depth-averaged velocity field at the Roompot inlet as shown in Figure 5. Values of the vorticity are shown for the same three stages of the tidal cycle (T_1, T_2, and T_3) that were used before, where blue denotes positive vorticity (i.e., counterclockwise rotation) and red denotes negative vorticity (i.e. clockwise rotation). As a reference, the transects sailed by the boat are included in red.

At time T_1 (Figure 8a), the vorticity is relatively small, the flow being more or less uniform in lateral direction without significant lateral gradients in the velocity field. At time T_2 (Figure 8b), the vorticity is relatively large and increases toward the scour hole. A possible explanation for this observation is the conservation of potential vorticity; along a streamline, the vorticity divided by the depth is constant. This will be elaborated on in section 4. At time T_3 (Figure 8c), vorticity is slightly smaller than at time T_2, though it is still significantly higher than at time T_1. Again, vorticity increases toward the scour hole.

The vertical vorticity component as computed from the interpolated depth-averaged velocity field at the Schaar inlet is shown in Figure 9 and shows similar patterns to those at the Roompot inlet. The increase of the vorticity at the scour holes of both inlets suggests that contraction of the flow may be interpreted as being the result of vertical stretching of vorticity.

3.5. Interpretation of Flow Dynamics

In this section we discuss the observed flow phenomena at the ES-SSB. First, we conceptualize the observed structure of the flow and highlight the most important observations. Next, we discuss the formation and development of the large-scale recirculation zones and the turbulence directly downstream of the barrier

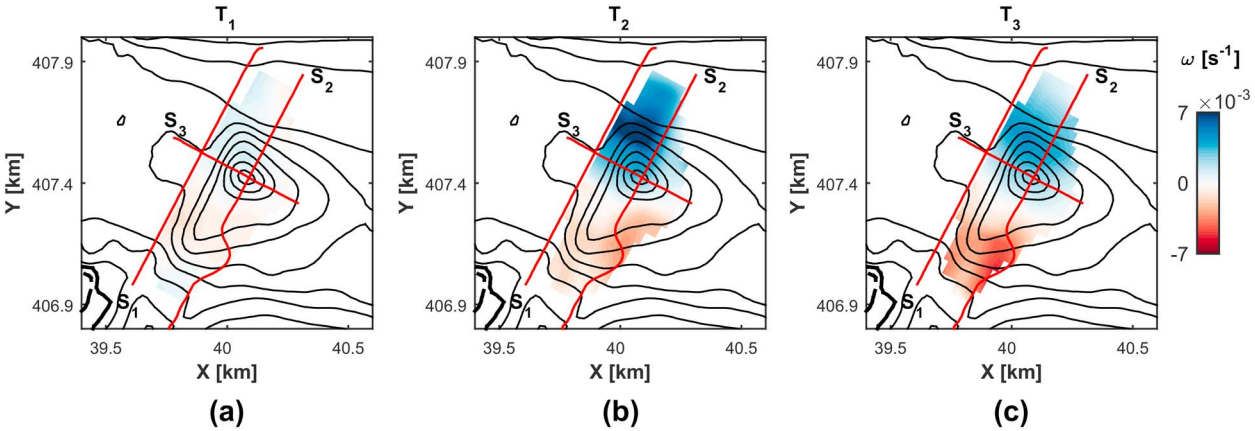

Figure 9. Vertical vorticity derived from the interpolated depth-averaged flow field at the Schaar inlet for three stages in the tidal cycle: 1.5 hr after slack tide (a), at maximum flood (b), and 1 hr after maximum flood (c). As a reference, boat transects S_1 – S_3 are plotted in red.

generated by the pillars. Finally, we discuss the shallowness of the large-scale phenomena to set up the framework for further analysis.

3.5.1. Conceptualization of the Types of Flow Structures

Two different types of flow structures were observed at the barrier, as shown schematically in Figure 10, for a simplified seabed morphology, with the scour hole represented as a uniformly sloping section without transverse variation. Figure 10a shows a flow with limited horizontal velocity differences upstream of the scour hole, which will vertically separate and diverge in the horizontal plane. The cross-sectionally averaged flow reduces proportionally to the depth increase (based on continuity arguments), with a corresponding deceleration of the flow in the core of the jet. Due to the vertical flow separation, velocities near the bed are relatively low.

Figure 10b shows a flow with large horizontal velocity differences upstream of the scour hole which will stay attached to the bed and converges in the horizontal plane. Again, based on continuity arguments, the cross-sectionally averaged flow velocity reduces proportionally to the depth increase, but due to the lateral contraction of the flow, the corresponding deceleration in the core of the jet is reduced, and lateral velocity differences remain high (or even grow). The vertical stretching of the horizontal jet structure and the accompanying horizontal contraction of the jet is similar to the vertical stretching of a single horizontal vortex. We exploit this analogy further in section 4.1. Due to the horizontal contraction, the flow remains attached, and near-bed velocities are relatively high.

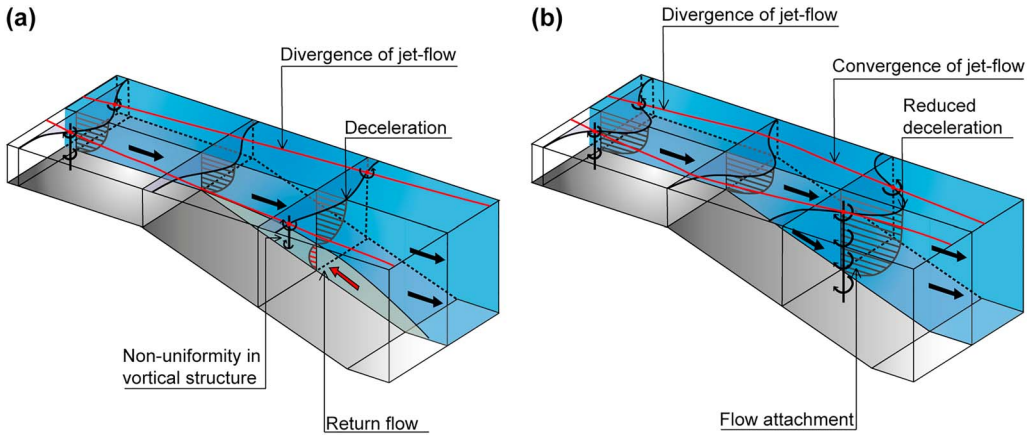

Figure 10. Conceptual sketch of the two different flow structures observed at the scour holes at the Eastern Scheldt Storm Surge Barrier: (a) a flow with limited horizontal velocity differences that is vertically separating and diverging in the horizontal plane; (b) a flow with large horizontal velocity differences that stays attached to the bed and converges in the horizontal plane. For both cases, the cross-sectionally averaged velocity reduces proportionally to the depth increase, but for a vertically separating flow (a), the deceleration of the core of the jet is far larger than for a flow that stays attached to the bed (b).

This link between the horizontal structure of the flow and the vertical structure of the flow will be further investigated in section 4.1.1.

3.5.2. Recirculation Zones

Observations of the flow at the Roompot and Schaar inlets show a jet-type flow structure induced by the local basin geometry upstream of the barrier. Recirculation zones were observed adjacent to the scour hole. The onset of growth of these recirculations does not occur immediately after slack tide: they start to grow once the lateral shear becomes larger, that is, when the lateral nonuniformity is larger. Another important contributor to the growth of the recirculation zones is the adverse pressure gradient caused by an overall deceleration of the flow at the scour hole due to the increase in conveyance cross section (Vermeulen et al., 2015). This deceleration is larger later on in the tidal cycle, when velocities on average are higher. It must be noted that even though on average the flow is decelerating above the scour hole, in the core of the jet, the deceleration is significantly less at some stages of the tidal cycle (Figure 10).

The observations suggest that the recirculation zones originate and develop at the beginning of the flood phase of the tidal cycle and do not influence the flow in the subsequent ebb phase. This is supported by considering the inlet Strouhal number K_W defined as $K_W = W/(U_m T)$, in which W is the inlet width, U_m the magnitude of the maximum cross-sectionally averaged tidal velocity, and T is the tidal period. For $K_W > 0.13$, the development of the jet vortex is arrested by the reversing tidal current, sweeping the emerging coherent structures back toward the inlet. For $K_W < 0.13$, the vortex formation induced by the accelerating jet is accomplished before the tidal current reverses, which effectively decouples the vortex dynamics between subsequent tidal cycles (Wells & van Heijst, 2003). We do note that the critical value of $K_W = 0.13$ was obtained for an idealized situation, while the actual critical value is also dependent on the shape of the inlet. Using estimated inlet widths of 1.0 and 1.5 km for the Schaar and Roompot inlets, respectively, a maximum cross-sectionally averaged tidal velocity of $U_m \approx 1$ m/s, and assuming an M_2 tide with a tidal period of 12 hr 25 min, the Strouhal numbers at the Schaar and Roompot inlets are equal to 0.02 and 0.03, respectively. Under the assumption that the order of magnitude of the critical value of K_W as predicted by Wells and van Heijst (2003) is correct, then the calculated values of K_W at the ES-SSB are an order of magnitude smaller, thus indicating detachment of the coherent structures. Therefore, we can safely say that the recirculation zones start developing at the beginning of the flood phase of the tidal cycle without being influenced by previously developed recirculating motions.

3.5.3. Wakes at the Barrier Openings

Upstream of the scour hole, aerial photographs revealed large turbulent structures on top of the base flow which are caused by flow separation at the barrier openings. The pillars of the barrier act as a grid, and the resulting flow pattern shows characteristics of grid turbulence (e.g., Uijttewaal & Jirka, 2003). Although the obtained data set does not provide any insight in the effect of the grid turbulence induced by the barrier pillars, a first-order estimate based on the size of the barrier pillars, their spacing, and the local water depth can be made. The bathymetry maps show that the water depth around the pillars, d, is approximately 20 m. For vortex shedding downstream of a cylinder, the typical length scale of the vortices is the width of the cylinder (Uijttewaal & Jirka, 2003). The width of a single pillar, D, is approximately 7.5 m, and the heart-to-heart distance between two pillars, D_p, is 45 m. Comparing the size of a single pillar with the local water depth of 20 m, two-dimensional horizontal dynamics like vortex merging are not expected in the wake of the pillars at the ES-SSB, since the local water depth is larger than the characteristic size of the vortices. Furthermore, the solidity of the grid, $S = D/D_p$, is relatively low ($S = 0.16$). Vortices that are shed form the pillars therefore remain separated from each other and dissipate before they have the opportunity to merge (Uijttewaal & Jirka, 2003). It is however possible that the grid-induced turbulence is an additional source of disturbances and vorticity promoting the generation and growth of a recirculation zone.

3.5.4. Shallowness of the Tidal Jet

On a larger scale, horizontal two-dimensionality of the flow may be of importance. As was mentioned in section 3.5.2, the cross-sectionally averaged flow velocity is decreasing above the scour hole, but this decrease is significantly less in the core of the jet at certain phases of the tidal cycle. Instead of spreading in lateral direction, which is commonly observed for tidal jets (e.g., Cohen, 2012), the jet is showing a different behavior: it contracts laterally toward the scour hole (Figure 10). As a result, the velocity difference above the scour hole remains relatively high in spite of the decrease in cross-sectionally averaged flow velocity (Tables 1 and 2). This leads to velocities in the scour hole that are larger than expected based on the increase in flow depth. To explain this behavior, we make use of the relative shallowness of the large-scale flow characteristics near the scour hole.

The width of the jets is approximated by the width of the inlets, so in the order of 1–1.5 km, while the water depth is in the order of tens of meters, therefore classifying the jet as a shallow jet (Jirka, 2001). Additionally, the horizontal extent of the recirculation zone is roughly 300–500 m, making the horizontal length scales of the large-scale flow phenomena significantly larger than the water depth. Moreover, the contracting behavior during particular stages of the tidal cycle is linked to a vertical structure of the flow that is approximately uniform (Figure 7b). To understand the contracting nature of the jet above the scour hole, a more detailed analysis of the large-scale flow structure will therefore be performed using a 2D-horizontal framework.

4. Analysis of Flow Dynamics

At the ES-SSB, during particular stages of the tide, we observe a flow with large lateral gradients of the streamwise velocity (and a corresponding high vorticity) experiencing a large local change in depth, the scour hole. As such, the important features of the flow may be understood through conservation of shallow water potential vorticity, resulting from conservation of angular momentum, which states that vorticity divided by the water depth is constant along a streamline. In this section we present the governing equations, and by formulating a simplified quasi-one-dimensional analytical model, we will explain the principal features of the observed flow characteristics.

4.1. Potential Vorticity Conservation

The conservation of potential vorticity is derived from the two-dimensional shallow water equations, given by the continuity equation,

$$\frac{\partial d}{\partial t} + \nabla \cdot \left(d\overline{\mathbf{u}} \right) = 0, \tag{2}$$

and the depth-averaged momentum balance,

$$\frac{\partial \overline{\mathbf{u}}}{\partial t} + \overline{\mathbf{u}} \cdot \nabla \overline{\mathbf{u}} + f\overline{\mathbf{u}}_{\perp} + g\nabla h = -\frac{1}{\rho d}\nabla \cdot \left(d\,\overline{\overline{\tau}}_t \right) - \frac{\bar{\tau}_b}{\rho d}, \tag{3}$$

in which d is the water depth, $\overline{\mathbf{u}}$ the depth-averaged velocity vector, f is the Coriolis parameter (chosen positive on the Northern Hemisphere), $\overline{\mathbf{u}}_{\perp}$ is the velocity vector rotated 90° counterclock wise, g is gravity, $\overline{\overline{\tau}}_t$ is the depth-averaged horizontal turbulence shear stress tensor, $\bar{\tau}_b$ is the bed shear stress, and ρ is the density of water. The symbol ∇ denotes the horizontal gradient operator. The closure of the system of equations (2) and (3) involves a parameterization of the bed shear stress and the turbulence stress tensor. The bed shear stress is often modeled using a quadratic friction law,

$$\bar{\tau}_b = \rho c_f |\overline{\mathbf{u}}| \overline{\mathbf{u}}, \tag{4}$$

in which c_f is a dimensionless bed friction coefficient. The turbulence shear stress is often assumed proportional to the horizontal gradient of the fluid velocity,

$$\overline{\overline{\tau}}_t = -2\rho \nu_t \nabla^s \overline{\mathbf{u}}, \tag{5}$$

in which ν_t is the turbulent viscosity, and $\nabla^s = \frac{1}{2}\nabla(\cdot) + \frac{1}{2}\nabla(\cdot)^T$ is the symmetric gradient operator.

A scaling argument shows that for the case of the ES-SSB, as a first approximation, the bed shear stress term and the turbulence stress term can be neglected with respect to the advective acceleration term in the momentum equation (3) if we consider a domain where the streamwise distance is of the same order as the width of the jet (i.e., the small distance assumption, see Appendix A). As a consequence, the right-hand side of the momentum equation (3) can be discarded. By taking the curl of the momentum equation (3) and using the continuity equation (2), the following equation for the depth-averaged vertical vorticity $\omega = \nabla \times \overline{\mathbf{u}}$ is obtained:

$$\left(\frac{\partial}{\partial t} + \overline{\mathbf{u}} \cdot \nabla \right) \left(\frac{\omega + f}{d} \right) = 0, \tag{6}$$

which states that the quantity $(\omega + f)/d$, the so-called potential vorticity, is constant when moving with the flow velocity $\overline{\mathbf{u}}$. We assume that background rotation is negligible, $f << \omega$, and that at the scale of the barrier, the local acceleration term is relatively small, so the flow can be considered (quasi-)stationary (Appendix A). Using an (s, n, z) coordinate system as defined in section 2.4, equation (6) further reduces to

$$u_s \frac{\partial}{\partial s}\left(\frac{\omega}{d} \right) + u_n \frac{\partial}{\partial n}\left(\frac{\omega}{d} \right) = 0, \tag{7}$$

in which u_s and u_n are the depth-averaged velocity components in the (s, n) coordinate system. For notational convenience, we have dropped the overbar. Equation (7) expresses that along a streamline, the vorticity ω is proportional to the water depth d. A consequence of this conservation law is that an initial lateral nonuniformity of the streamwise velocity may experience an increase once the flow enters a deeper region. With the purpose of characterizing the behavior of a jet-type flow over a sloping bed as at the ES-SSB, we seek approximate solutions to the equation of potential vorticity conservation (7). To that end, we assume that the velocity component in lateral direction (u_n) is much smaller than the velocity component in streamwise direction (u_s). This assumption implies that streamlines are approximately straight, which is a reasonable first approximation based on the field data. The lateral boundaries of the domain are slip boundaries, which is consistent with the assumption of inviscid flow. At the inflow boundary, the streamwise velocity field as obtained from a known streamwise velocity profile is imposed:

$$u_0(n) = u_s(0, n), \tag{8}$$

from which the corresponding vorticity at the inflow boundary is obtained by calculating the derivative of the streamwise velocity in n direction:

$$\omega_0(n) = \frac{\partial u_0}{\partial n}. \tag{9}$$

As we assumed the streamlines to be straight and using equation (7), the vorticity at any location in the domain is given by

$$\omega(s, n) = \frac{d(s, n)}{d(0, n)}\omega_0(n). \tag{10}$$

The corresponding streamwise velocity is obtained after integration of equation (10) in the n direction, giving

$$u(s, n) = \frac{d(s, n)}{d(0, n)}u_0 - \int \left[u_0 \frac{\partial}{\partial n}\left(\frac{d(s, n)}{d(0, n)}\right)\right] \mathrm{d}n + C. \tag{11}$$

The integration constant C is determined by the requirement that the total mass flux through each cross section is constant:

$$\int_{n_L}^{n_U} u(s, n)d(s, n)\mathrm{d}n = \int_{n_L}^{n_U} u_0 d_0 \ \mathrm{d}n; \tag{12}$$

where n_L is the lateral coordinate of the lower lateral boundary of the domain, and n_U is the lateral coordinate of the upper lateral boundary of the domain.

To be able to find an analytical solution to equation (7), we assumed small lateral velocities. These may be computed using equation (2) as a postprocessing step. We remark that by taking the curl of the shallow water equations, the pressure term is eliminated, reducing equation (7) to be purely kinematic. The corresponding pressure distribution may be solved by substitution of the velocities computed from potential vorticity conservation in the shallow water equations.

4.1.1. Depth Uniformity

The conservation of potential vorticity, as derived above, is valid for a 2D-horizontal situation, (thus implicitly) assuming a vertically uniform flow. However, for a sloping bathymetry, vertical flow separation may occur if the steepness of the slope is large enough, which would violate the assumption of depth uniform flow. The velocity data suggest a link between the presence of lateral nonuniformities in the velocity distribution and vertical attachment of the flow, which will be investigated in this section.

Vertical flow separation occurs when the boundary layer detaches from the bed (Simpson, 1989), often as a result of a pressure gradient acting against the flow direction (Vermeulen et al., 2015) due to deceleration of the flow in a region of flow expansion, as for instance in a scour hole. Equation (11) implies that through the conservation of potential vorticity, the flow at such a topographic expansion may locally experience an additional streamwise acceleration, which may lead to a reduced deceleration in the core of the jet, see Figure 10. It is hypothesized that this acceleration may suppress the adverse pressure gradient resulting from an increase in conveyance cross section, such that the bottom boundary layer stays attached to the bed. We will show that the flow may stay attached to the bed when lateral nonuniformities, expressed as the relative lateral velocity difference $\Delta u/u_a$, are present in the flow.

In this analysis, the effect of the free-stream pressure gradient, which is related to the change in free-stream velocity, is used to determine a critical steepness of the bed slope for which boundary layer separation is

expected. The change in free-stream velocity is related to the bed slope, and using boundary layer theory, we can deduce that a critical deceleration of the flow is some function of the bed shear stress and the boundary layer characteristics (e.g., Chang, 1970). Therefore, by expressing the change in free-stream velocity in terms of the bed slope, we can define a critical bed slope for which boundary layer separation is expected to occur. We can do this for a laterally uniform flow and for a laterally nonuniform flow. For a laterally nonuniform flow, we envision that there is, locally, an additional acceleration through horizontal contraction of the flow resulting from conservation of potential vorticity, leading to a reduction of the adverse free-stream pressure gradient. Therefore, we expect vertical flow separation to occur for a different, steeper critical bed slope ($i^*_{b,c}$) compared to the critical bed slope for which vertical flow separation is expected for a laterally uniform flow ($i_{b,c}$). By assessing the difference in free-stream pressure gradient for a laterally uniform and a laterally nonuniform flow, we can relate the presence of lateral velocity differences to a steepening of the critical bed slope, which is expressed as

$$\frac{i^*_{b,c}}{i_{b,c}} \propto \left(1 - \alpha \frac{\Delta \tilde{u}_0}{\tilde{u}_{a,0}}\right)^{-1}, \tag{13}$$

where the tildes denote the free-stream velocities, the subscript 0 denotes the velocities at the edge of the slope, and α is a constant parameter of $\mathcal{O}(1)$, accounting for the shape of the velocity profile, the length scale of the mixing layer, and the lateral extent of the scour hole. The full derivation of equation (13) can be found in Appendix B1. We consider the measured depth-averaged values of the velocity difference (Δu_0) and cross-sectionally averaged velocity ($u_{a,0}$) to be approximately equal to their free-stream counterparts, the only difference being in the boundary layer contribution.

Equation (13) expresses that for a larger relative (free-stream) velocity difference $\Delta \tilde{u}_0/\tilde{u}_{a,0}$ at the edge of the slope, the boundary layer may stay attached for a steeper slope than for the case of a laterally uniform flow velocity. This appears to be consistent with our hypothesis based on the field observations: if the additional acceleration as a result of potential vorticity conservation is large enough, flow may stay attached to the bed. Tables 1 and 2 show that at time T_1, when vertical recirculation currents were observed at the scour hole, the relative velocity difference is the smallest and decreasing toward the scour hole. Later on in the tidal cycle, the relative velocity difference is higher and increasing toward the scour hole. During these stages of the tidal cycle, the flow is approximately depth uniform. Therefore, we expect the model to be valid for situations where the relative velocity difference is large enough, which is the case at the ES-SSB most of the time.

4.2. Idealized Model Application: Linearly Sloping Bed

In this section the idealized model is applied to gain insight in the behavior of a jet that experiences an increasing water depth. For this analysis, we assume that the relative velocity difference of the jet at the inflow boundary is large enough with respect to the bed slope (i_b), so vertical flow separation is counteracted. We apply equation (11) to an idealized bathymetry, a linearly sloping bed that is uniform in n direction over the entire width B of the domain (LS model) with the depth given by

$$d(s,n) = d_0 + i_b s, \tag{14}$$

in which d_0 is the depth at the inflow boundary, and i_b is the slope of the bed. This specific bathymetry allows for an analytical solution of equation (7), which nevertheless illustrates the principal behavior of the considered flow phenomena.

At the inflow boundary, a jet-type velocity profile is prescribed which is well approximated by a Gaussian (Dracos et al., 1992):

$$u(0,n) = u_c \exp\left[-\frac{n^2}{2\sigma^2}\right], \tag{15}$$

in which u_c is the magnitude of the centerline velocity of the jet at the inflow boundary ($s = 0$), and σ is a measure of the width of the jet, with the requirement that the jet flow velocity at the inflow boundary ($s = 0$) is negligible at the lateral boundaries n_L and n_U (i.e., $\sigma = B/6$). An analytical expression for the streamwise velocity now reads

$$u(s,n) = \gamma u_c \exp\left[-\frac{n^2}{2\sigma^2}\right] + \sqrt{2\pi} u_c \sigma \left(\gamma^{-1} - \gamma\right) B^{-1}, \tag{16}$$

in which $\gamma = d(s,n)/d_0$ is the relative depth increase with respect to the depth at the inflow boundary. The derivation of equation (16) is given in Appendix B2. Equation 16 is a solution to equation (7) for the bathymetry given by equation (14) and the boundary condition given by equation (15). Equation (16) shows

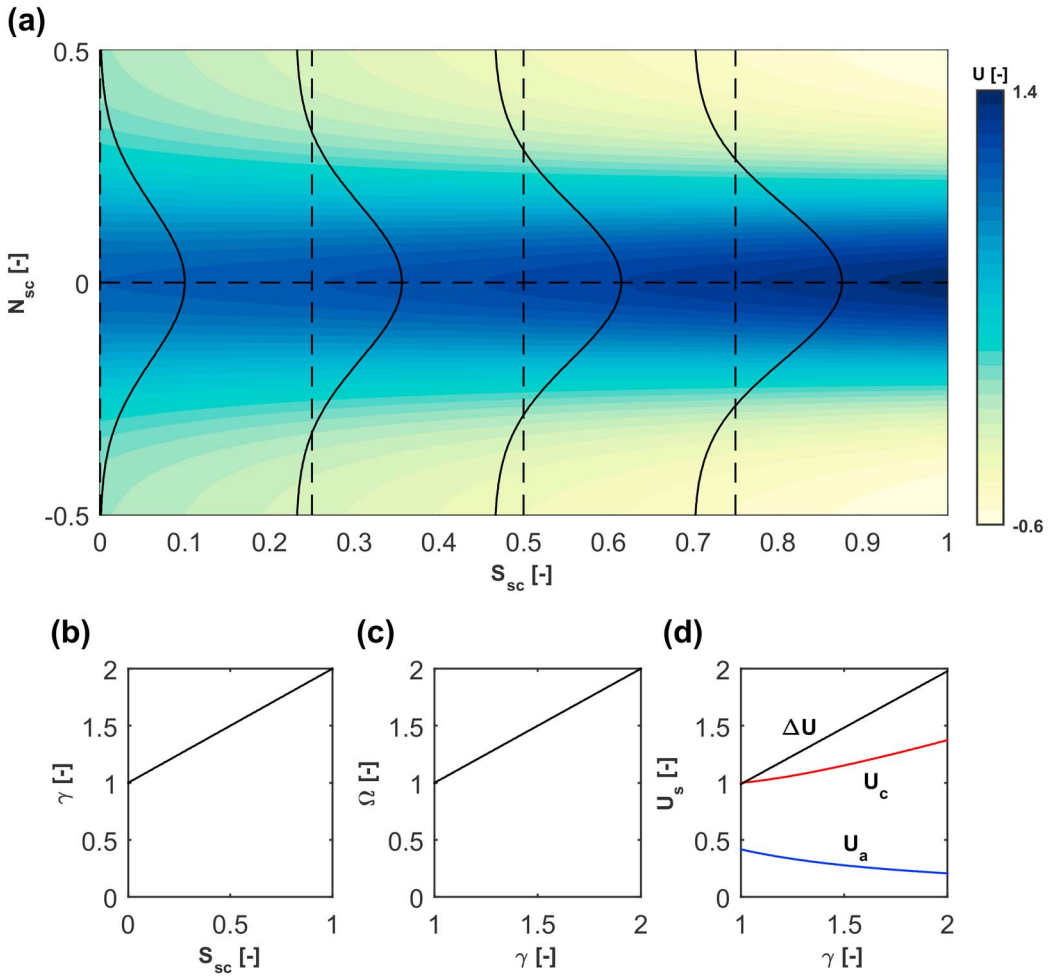

Figure 11. Results of the analytical model. (a) Streamwise velocity through the domain, black solid lines are velocity profiles at locations indicated with the black-dotted lines; (b) relative depth increase γ as a function of streamwise distance S_{sc}; (c) maximum vorticity Ω as a function of the relative depth increase γ; (d) average velocity (blue), centerline velocity (red) and velocity difference (black) as a function of the relative depth increase γ.

that the streamwise velocity is a function of the relative depth increase γ, irrespective of the bed slope i_b. Therefore, we eliminate the dependency on streamwise distance by presenting the results of the analytical model (equation (16)) using the following scaled quantities: $S_{sc} = s/B$, $N_{sc} = n/B$, $U(S_{sc}, N_{sc}) = u(s,n)/u_c$, $\Omega = \omega(s,n)_{\max}/\left|\omega_0\right|_{\max}$, and γ). We use the scaled quantities to assess the change of the cross-sectionally averaged flow velocity U_a, the lateral velocity difference over the domain ΔU, and the relative velocity difference $\Delta U/U_a$ relative to the change in water depth. We are considering a (scaled) streamwise distance that is equal to the width of the jet to satisfy the model assumption of a relatively small streamwise distance. Referring to the ES-SSB, this is approximately the width of the inlet, and it covers a streamwise distance that includes the bed protection and the scour hole. The maximum depth that we consider here is twice the depth at the inflow boundary, which is the same order of magnitude as at the ES-SSB.

Figure 11 shows the results of the model for a relative depth increase γ of 2. Figure 11a shows that the velocity in the center of the domain is increasing despite the increasing depth, which is a result of the flow contracting toward the center of the domain. This is due to the increasing maximum vorticity, Ω (Figure 11c), proportional to the relative increase in depth, γ (Figure 11b). As a result, the velocity difference ΔU increases in proportion to the relative depth increase as well, as can be seen in Figure 11d. The cross-sectionally averaged flow velocity, U_a, is decreasing proportionally to the relative depth. In the center of the domain, the combination of deceleration of the average flow velocity and acceleration due to contraction of the flow leads to a net increase in centerline velocity, U_c (Figure 11d, red line). The relative velocity difference, $\Delta U/U_a$, increases for an increase in water depth.

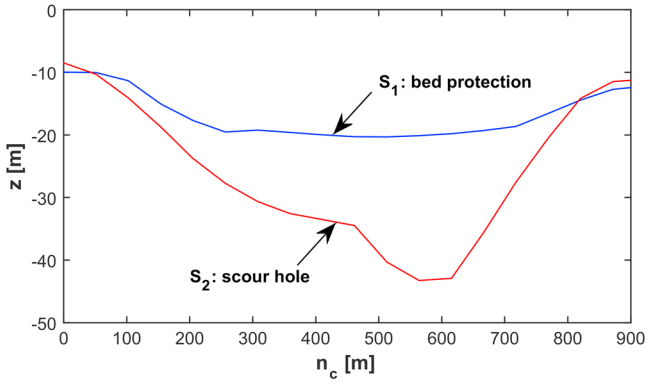

Figure 12. Bathymetry at transects S_1 (blue) and S_2 (red) as used in the model.

The decrease of cross-sectionally averaged velocity, U_a, in combination with an increase of relative velocity difference, $\Delta U/U_a$, for an increasing water depth is a phenomenon that was observed in the velocity data collected at the ES-SSB (see Tables 1 and 2). As such, the conservation of potential vorticity may explain the observed behavior of the flow at the ES-SSB during particular stages of the tidal cycle, that is, when the lateral velocity differences are large enough. If the jet satisfies these conditions, a converging character rather than a diverging character is expected.

4.3. Model Application: Schaar Inlet

Now we apply the general model formulation to the flow at the Schaar inlet to assess the hypothesis that potential vorticity conservation for a large part governs the observed large-scale behavior of the flow at the ES-SSB. The Schaar inlet was chosen because the transects sailed by boat with the ADCP ($S_1 - S_3$) cover the width of the entire inlet, so determining the total mass flux through a cross section is more accurate than at the Roompot inlet.

The model domain is confined between transects S_1 (above the bed protection, parallel to the barrier) and a transect parallel to the barrier at the downstream end of the scour hole, S_2. Transect S_1 is defined as the inflow boundary. The water depths along transect S_1 and transect S_2 are plotted in Figure 12. The coordinate n_c denotes the distance along the transect. The observed transverse profile of streamwise velocity measured at S_1 is applied as a boundary condition at S_1. The horizontal distance between the transects is approximately 300 m, which is one third of the inlet width, so the small distance assumption is satisfied. The straight streamline assumption is reasonable in the center of the domain, but not on the outer sides of the domain (Figure 6). However, as can be seen in Figure 9, the vorticity at the sides of the domain is relatively small, so we expect the contribution from shear, $\partial u/\partial n$, to be the dominant source of vorticity at the ES-SSB.

The vorticity field in streamwise direction was computed by solving equation (10) assuming straight streamlines and using a (simple) Euler forward space-marching scheme, with a step size of 15 m. Subsequently, the velocity can be computed by integration of equation (10) and applying equation (12).

Figure 13 compares observed (Figures 13a – 13c) and computed (Figures 13d – 13f) vorticity at the Schaar inlet for three stages of the tidal cycle: 1.5 hr after slack tide, (T_1, Figures 13a and 13d), at maximum flood (T_2, Figures 13b and 13e), and 1 hr after maximum flood (T_3, Figures 13c and 13f). Figure 14 shows the resulting computed transverse profiles of the streamwise velocity along transect S_2 compared with the corresponding observations. Table 3 lists observed and computed values of the cross-sectionally averaged streamwise velocity u_a, the horizontal velocity difference over the transect ΔU, and relative velocity difference $\Delta u/u_a$ at transects S_1 and S_2.

For all three stages in the tidal cycle, the model predicts increasing vorticity and high velocities above the scour hole and increasing lateral velocity differences. This behavior is in most cases in agreement with observations.

At T_1, the computed vorticity (Figure 13d) does not show the same patterns as the observed vorticity (Figure 13a). The discrepancy between model computation and field observations is easily explained. At this stage of the tidal cycle the relative velocity difference is the lowest (Table 3). As a result, there is little to none acceleration of the flow due to potential vorticity conservation. As a result, the flow in the center of the jet cannot overcome the critical adverse pressure gradient causing vertical flow separation (equation (13)). As was mentioned in section 3, at T_1, a vertical return flow was observed in the data, violating the model assumptions at this stage of the tidal cycle.

At T_2, the computed vorticity (Figure 13e) shows a pattern that is more similar to the observed vorticity (Figure 13b). In the southern part of the domain, the location of peak vorticity is computed well, but the magnitude is slightly too high. As can be seen in Figures 14c and 14d, this leads to a slight shift of the peak velocity toward the south. The magnitude of the vorticity in the northern part of the domain is computed fairly well, but the location of the maximum is shifted slightly toward the south. Therefore, the lateral gradient in the velocity profile is too steep. The magnitude of the peak velocity above the scour hole is predicted

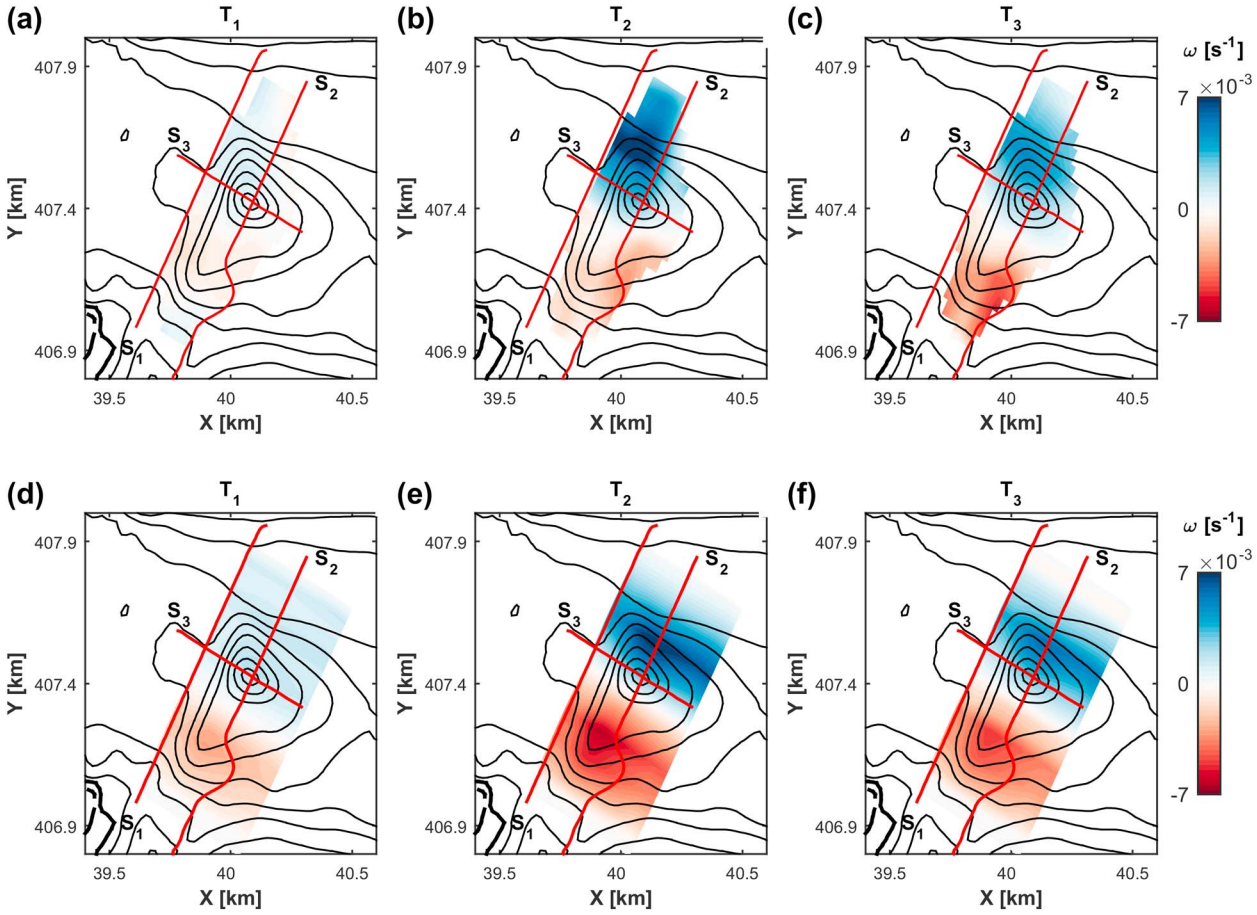

Figure 13. Observed (upper panels) and computed (lower panels) vorticity at the Schaar inlet at T_1 (a and d), T_2 (b and e), and T_3 (c and f).

accurately by the model (see Table 3). The model computes the cross-sectionally averaged velocity and the velocity difference over the cross section well.

At T_3, the similarity between computed (Figure 13f) and observed (Figure 13c) vorticity is the highest. The patterns of increasing vorticity above the scour hole are represented fairly well by the model, and location of peak vorticity is predicted accurately by the model. The magnitude of the vorticity is computed well. The increasing magnitude of vorticity in streamwise direction above the scour hole leads to an increase in lateral velocity differences in the transverse velocity profile, which the model is able to capture (Figures 14e and 14f). The location and magnitude of the maximum streamwise velocity is accurately reproduced by the model. Again, Table 3 shows that the model is very well capable of predicting the cross-sectionally averaged velocity and the velocity difference over the cross section. The model has the tendency to mostly overpredict positive vorticity, whereas negative vorticity is generally computed more accurately. This asymmetry toward positive vorticity may potentially be explained by the presence of the harbor in the southern part of the domain that is drawing part of the flow. However, our data resolution in this area is not sufficient to give a definite answer to this issue, so for now this remains unresolved.

Although there are some discrepancies between model computations and field observations, for the cases where the relative velocity difference is large enough, and flow stays attached to the bed, the model is very well able to reproduce the relevant phenomena. This is consistent with our expectations based on equation (13). Based on more traditional considerations, one would expect the flow velocity to decrease in proportion to the depth increase, which would lead to a significant velocity reduction above the scour hole. Instead, conservation of potential vorticity appears to be dominant in shaping the horizontal structure of the flow; due to an increase in water depth, the vorticity increases proportionally. As a result, the jet shows a

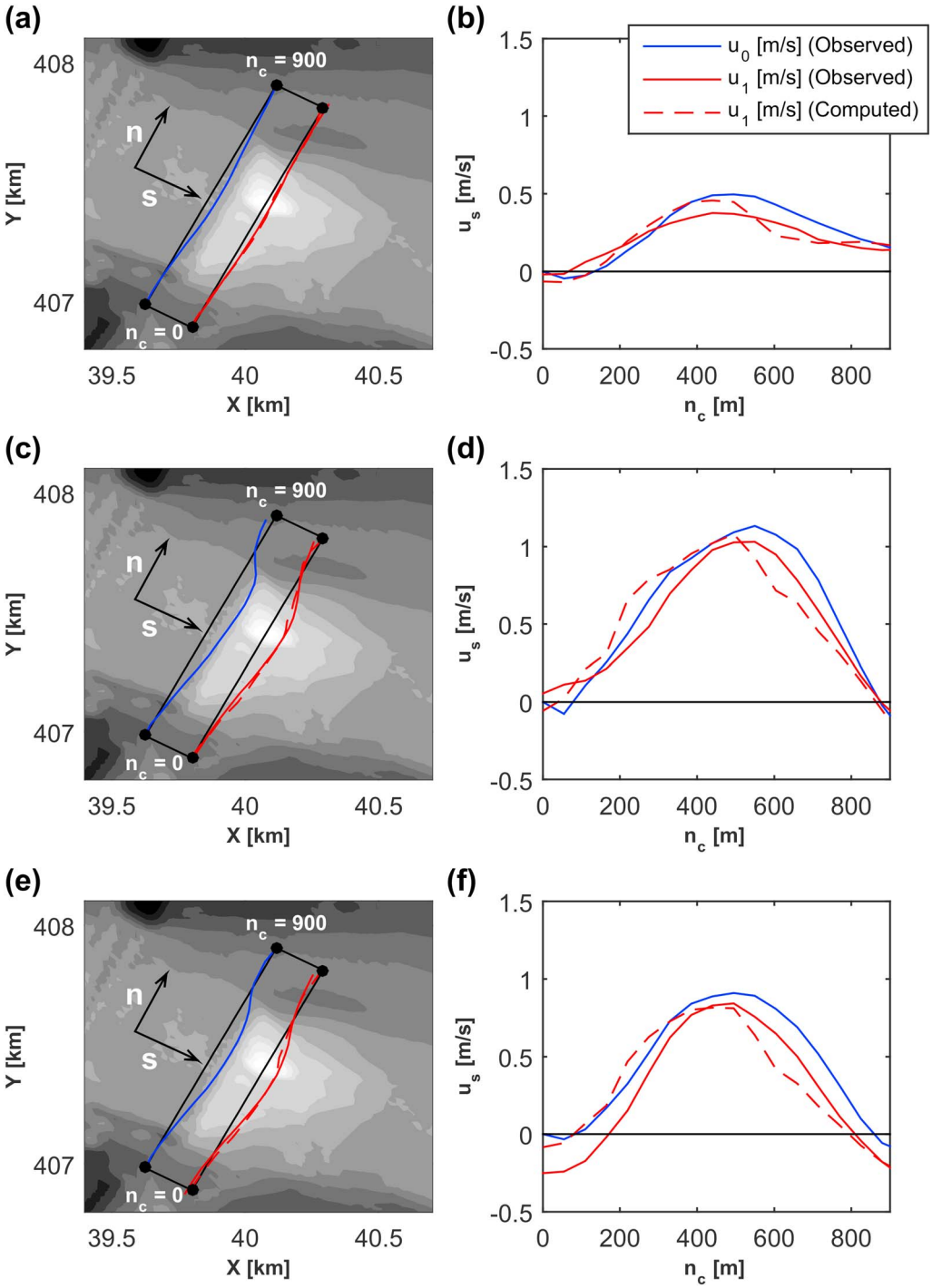

Figure 14. Observed (blue solid line) velocity at inflow transect S_1 and observed (red solid line) and computed (red-dotted line) streamwise velocity at transect S_2 at the Schaar inlet. Results are shown 1.5 hr after slack (a and b), at maximum flood (c and d), and 1 hr after maximum flood (e and f).

converging character toward the deepest part of the scour hole, as opposed to spreading laterally, maintaining relatively high velocities in the deeper part of the scour hole.

4.4. Consequences for the Scour Hole Development

Field observations of the flow at the ES-SSB revealed a jet-like structure of the flow downstream of the barrier. During particular stages of the tide, flow was observed to contract toward the deepest part of the scour hole. It was shown that this behavior occurs when the lateral nonuniformity of the flow becomes larger. For larger

Table 3
Values of u_a, Δu, and $\Delta u/u_a$ Along Transects S_1 and S_2 at the Schaar Inlet

	Transect	u_a (m/s)	Δu (m/s)	$\frac{\Delta u}{u_a}$ (–)
T_1: 1.5 hr after slack	S_1: Observed	0.26	0.56	2.12
	S_2: Observed	0.22	0.42	1.83
	S_2: Computed	0.22	0.59	2.68
T_2: maximum flood	S_1: Observed	0.46	1.97	3.00
	S_2: Observed	0.31	1.37	4.42
	S_2: Computed	0.35	1.49	4.26
T_3: 1 hr after maximum flood	S_1: Observed	0.36	1.04	2.89
	S_2: Observed	0.20	1.15	5.75
	S_2: Computed	0.22	1.22	5.55

Note. Both observed and computed values are shown.

lateral nonuniformities, the contraction of the flow becomes larger, and vertical flow separation may be suppressed. As a consequence, highest flow velocities were found directly above the scour hole, in combination with steep gradients at the sides of the jet and high downward-directed vertical velocities near the bed in the center of the jet. This flow structure is likely to have a large impact on the ongoing scour process.

The combination of vertical flow attachment and enhanced contraction makes that high streamwise momentum can be advected to the bed. This may subsequently induce high bed shear stresses and thus significantly contribute to the scouring process. At the interface of the main flow and the horizontal recirculation zone, turbulence intensities will be high since large gradients facilitate development and growth of instabilities into large eddies. Upon closer inspection of the bathymetry, it appears that the maximum scour depths are not necessarily found in the center of the domain but more to the sides of the channel where horizontal velocity gradients are high. Additionally, the higher velocity gradients allow for a larger exchange between the main flow and recirculation zone, leading to a larger growth of the horizontal recirculation zone. The presence of the fully developed recirculation zones contributes to the high velocities in the center of the channel by reducing the conveyance cross section. Therefore, high velocities and the accompanying high bed shear stresses may persist for a longer time, increasing the scour potential.

The observed enhanced contraction and the accompanying large velocity gradients at the ES-SSB are a manifestation of potential vorticity conservation, and they were shown to be proportional to the relative depth increase. Therefore, the scour potential may remain high as the scour depth progresses, thus revealing a positive feedback mechanism where in certain conditions the scour development can be self-amplifying. Obviously, this process will not continue forever. Either the depth or the slope of the scour hole will become so large that flow velocities will become lower than the sediment entrainment threshold or flow will simply separate again. However, the equilibrium depth in intrinsically three-dimensional situations may be significantly larger than the equilibrium depth in a flow that can be considered as 2D-vertical.

5. Discussion

Flow velocity data at the ES-SSB revealed an intricate flow structure during particular stages in the tidal cycle, featuring attachment of flow to the bed in combination with a convergence of streamlines in the horizontal plane (Figure 10). We found this attachment-convergence behavior of the flow to be analogous to that of the vertical stretching of a single vortex and exploited this analogy by setting up a simple model based on conservation of shallow water potential vorticity. The purpose of this model was to understand the large-scale characteristics of the flow structure at the ES-SSB, rather than to serve as a predictive tool. The main advantage of the model that we used is that it explicitly relates horizontal nonuniformity of the flow and topographic variability in a very intuitive way, and we have demonstrated that this can for a large part explain the observed behavior of the flow at the ES-SSB. We do note, however, that reality is far too complex to be captured entirely by this very simple approach.

We have assumed an inviscid flow, where the effect of bed friction is not accounted for. Another implication of assuming inviscid flow is that there is no interaction between steepening of the lateral gradient on the one hand and the impact this has on fluid entrainment and mixing of the jet on the other hand (e.g., Turner, 1986). Moreover, generation (or destruction) of potential vorticity due to a jump discontinuity in the bed as described by Brocchini (2013) was not taken into account. We have additionally assumed that lateral velocities are much smaller than streamwise velocities, such that the second term of equation (7) vanishes. A scaling argument easily shows that this assumption is reasonable for relatively small distances (see Appendix A), but especially at the steep side slopes of the scour hole, this may not be the case. Finally, Falcini and Jerolmack (2010) have shown that high sediment concentrations may slightly alter the potential vorticity in a jet. The sediment concentration in the jet as it reaches the edge of the bed protection is relatively low, as there is barely any sediment to pick up from the bed protection mats. However, above the scour hole, the sediment concentration may change considerably, which was left out of consideration in this study.

Nevertheless, despite its limitations, the model was very well able to reproduce the relevant large-scale flow phenomena. The main strength of the model is that due to its simplicity, it provides a very intuitive way to interpret the observed stretching-contraction behavior of a laterally nonuniform flow that experiences a streamwise increase in depth. This insight applies to many other (similar) situations in riverine and coastal environments where deep scour occurs in combination with a flow with large horizontal velocity differences.

6. Conclusions

In this study, the depth-averaged flow structure at scour holes downstream of hydraulic structures with a bed protection was investigated. The ES-SSB was chosen as a case study. At this location, large scour holes have developed downstream of the applied bed protection, with local water depths of approximately 60 m, associated with roughly 40 m of scour. Field observations showed that the flow at the barrier has a jet-like structure, with the presence of large-scale quasi two-dimensional recirculating motions adjacent to the scour. However, instead of spreading laterally, the jet was shown to contract more toward the deepest part of the scour hole. The local (scour) bathymetry plays an important role in shaping the structure of the flow as observed, which may be understood from considering conservation of potential vorticity in a 2D-horizontal framework: for an increasing water depth, the vorticity should increase proportionally, explaining the contracting nature of the flow. As a result, the cross-sectionally averaged velocity decreases proportionally to the increase in water depth, but the velocity difference over the cross section remains relatively high. However, if vertical flow separation occurs on the upstream slope of the scour hole, depth uniformity does not hold anymore, and at these moments, a more diverging character of the jet was observed.

Taking into account lateral nonuniformity of the flow is crucial in understanding the observed phenomena. Vertical flow separation may be suppressed for a larger initial relative velocity difference over the cross section: through potential vorticity conservation, the flow may locally experience an additional acceleration, and as a result, the adverse pressure gradient that is responsible for separation of the boundary layer from the bed is reduced. The field observations support this notion: when the relative velocity difference over the cross section is smaller, vertical flow separation was observed, whereas for a larger relative velocity difference, the flow was observed to stay attached to the bed. So, for larger lateral nonuniformities in the horizontal structure of the flow, the vertical structure of the flow appears to become more depth uniform. The precise mechanisms behind this interaction are the topic of ongoing research. For now, it is concluded that a two-dimensional modeling approach as was used in this study is not necessarily the best option, as it is the mutual interaction of the vertical and the horizontal structure of the flow that determines the character of the flow.

A flow structure with concentrated high velocities and large lateral gradients is likely to contribute to the ongoing scour development. Through the downward-directed vertical flow, high streamwise momentum can be advected to the bed, potentially leading to high bed shear stresses. As the enhanced contraction of the flow is proportional to the relative increase in depth, the scour bathymetry itself is crucial in shaping this contracted flow structure. A positive feedback mechanism is thus revealed; lateral velocity gradients lead to relatively high near-bed velocities in the scour hole via horizontal flow contraction, which likely enhances erosion—causing an even stronger horizontal contraction—and maintains the scouring potential. Therefore, taking into account the three-dimensionality of the flow structure explains the larger growth of a scour

hole than what would be expected based on two-dimensional vertical modeling. This work inspires further experimental and numerical studies to the three-dimensional character of the phenomena.

Appendix A: Scaling: Small Distance Assumption

The following scale variables are introduced: a horizontal length scale $s, n \sim L$, a vertical length scale $z \sim H$, a time scale $t \sim T$, and a velocity scale $\bar{\mathbf{u}} \sim U$. It was shown by Jirka and Seol (2010), based on a scaling argument, that in shallow flows, the bottom friction term dominates over the turbulence diffusion term, as long as the turbulence diffusivity is governed by bottom shear. At the ES-SSB, the turbulence diffusivity from horizontal mixing is larger than the diffusivity by bottom shear due to the large lateral gradients in the flow. The turbulence viscosity is estimated using the Prandtl-mixing length hypothesis:

$$\nu_t = l_m^2 \left| \frac{\partial u}{\partial n} \right|. \tag{A1}$$

The mixing length l_m in free shear layers can be assumed constant across the layer and proportional to the local mixing layer width (Rodi, 1980). For a plane jet, the proportionality constant is 0.09, and the mixing layer width, W, is approximately the jet width. We now consider a horizontal length scale L that is of the same order of magnitude as the jet width W, and thus, the advective acceleration dominates over the turbulent diffusion by a factor of $0.09^{-2} (\approx 123)$. Values of c_f for field situations are of order $\mathcal{O}\left(10^{-3}\right)$, the water depth is of order $\mathcal{O}\left(10^{1}\right)$, and the horizontal length scale is of order $\mathcal{O}\left(10^{2} - 10^{3}\right)$; thus, the advective acceleration dominates over the friction by a factor of 10–100.

The ratio between the advective acceleration to the local acceleration is of the order $\mathcal{O}(UT/L)$. We consider the typical time scale T to be the period of the M_2 tide, which equals 12 hr 25 min, the typical velocity scale $U \approx 1$ m/s, and we take for the horizontal length scale again the width of the jet, W. Then the advective acceleration dominates over the local acceleration by a factor of approximately 50.

The background rotation due to Coriolis, f, is given by

$$f = 2\omega_e \sin(\phi), \tag{A2}$$

in which $\omega_e = 0.729 \cdot 10^{-4}$ rad/s is the angular frequency of the rotation of the Earth, and $\phi = 51°$ is the latitude of the Eastern Scheldt estuary. This yields a value of $f \approx 1 \cdot 10^{-5}$, which is approximately 100 times smaller than the vorticity at the ES-SSB.

The small distance assumption has implications for another assumption as well. In equation (7), which is repeated here:

$$u_s \frac{\partial}{\partial s}\left(\frac{\omega}{d}\right) + u_n \frac{\partial}{\partial n}\left(\frac{\omega}{d}\right) = 0, \tag{A3}$$

we have assumed that the second term is small w.r.t the first term on the argument that the lateral velocities are much smaller than the streamwise velocities. However, when the bed varies in n direction as well, this does not necessarily have to be true. A scaling argument shows the necessary conditions for which we can drop the second term in equation (7). We choose velocity scales $u_s, u_n \sim U, V$, length scales $s, n \sim L_s, L_n$ where L_s is a length scale for the streamwise direction and L_n a length scale for the side slope, a depth scale $d \sim H$ and a vorticity scale $\omega \sim U/\delta$, with δ the mixing layer width. Then, equation (7) scales accordingly:

$$\frac{U^2}{L_s \delta H} + \frac{UV}{\delta L_n H} = 0, \tag{A4}$$

which simplifies to

$$\frac{U}{L_s} + \frac{V}{L_n} = 0. \tag{A5}$$

This equation states that, given that $V << U$, that the second term is important only if $L_n << L_s$. So, the length scale of the side slope (which is a measure of its steepness) should be very small compared to the streamwise distance. We consider a streamwise distance of approximately 300 m, and a representative distance for the side slope is approximately 300 m as well. The data show that it is a reasonable assumption that $V \approx 0.1U$ for most of the time, with extremes to $V \approx 0.25U$. Therefore, the assumption that term 2 of the left-hand side of equation (7) is small w.r.t. term 1 is fair, though care has to be taken.

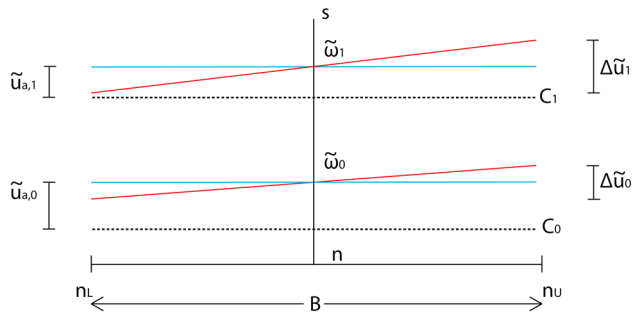

Figure B1. Sketch of the situation considered: at two different streamwise locations C_0 and C_1 with respective depths d_0 and d_1, the transverse profile of the streamwise velocity is plotted for a laterally uniform case (blue) and a laterally nonuniform case (red).

Appendix B: Model Derivations

B1. Derivation of the Depth-Uniformity Criterium

We assume that the free-stream velocity ($\tilde{u}$) is a known function of the streamwise distance s. With a known free-stream velocity, the momentum balance across the thickness of the boundary layer can be described using the Von Karman momentum integral equation (e.g., Chang, 1970):

$$\frac{d}{ds}\left(\tilde{u}^2\theta\right) = \frac{\overline{\tau_b}}{\rho} - \tilde{u}\frac{d\tilde{u}}{ds}\delta^*, \tag{B1}$$

where θ is the thickness of the boundary layer accounting for momentum transport (momentum thickness), and δ^* is the thickness of the boundary layer accounting for mass transport (displacement thickness) as defined in Chang (1970).

In equation (B1), the term on the left-hand side represents the development of the amount of momentum in the boundary layer. The increase or decrease of momentum in the boundary layer is dependent on bed shear stress, which is the first term on the right-hand side, and the pressure gradient, which is the second term on the right-hand side. Boundary layer separation along the slope will occur if the amount of momentum in the boundary layer becomes zero. To annihilate the momentum in the boundary layer, the pressure gradient along the slope, which can be related to the streamwise change in free-stream velocity, must exceed a critical value over a certain streamwise distance. By comparing the pressure gradient for a laterally uniform and a laterally nonuniform flow and relating that pressure gradient to a bed slope, we derive an equation that relates lateral velocity differences to a steepening of the slope for which vertical flow separation is expected.

Figure B1 is an idealized sketch of the situation. At two different positions along the streamwise direction (C_0 and C_1), a transverse cross section over the domain width B is considered (black-dotted line). The lateral coordinates of the lower lateral boundary and the upper lateral boundary are denoted by n_L and n_U, respectively. Along cross-section C_0, the depth equals d_0, and along cross-section C_1, the water depth equals $d_1 > d_0$. We assume that the depth increases linearly from d_0 to d_1, such that $\Delta d/\Delta s \approx i_b$. At cross-section C_0, the streamwise velocity of the laterally nonuniform flow (red line) is known and thus the velocity difference over the profile, $\Delta\tilde{u}$, and the vorticity, $\tilde{\omega}$. In blue, the cross-sectionally averaged flow velocity, $\tilde{u_a}$, is shown. The flow velocity of the laterally uniform case is chosen such that it equals the cross-sectionally averaged flow velocity of the nonuniform flow.

We start by deriving the deceleration of the flow for the laterally uniform case. The low Froude number values observed allow the use of the rigid lid assumption, such that the flow velocity of the laterally uniform 2D-vertical case is a function of the water depth (conservation of mass):

$$\tilde{u}_a(s) = \frac{\tilde{u}_{a,0}d_0}{d(s)}. \tag{B2}$$

For a linearly sloping bed, the deceleration along the slope is now

$$\frac{d\tilde{u}_a(s)}{ds} = -\frac{\tilde{u}_{a,0}d_0}{d(s)^2}i_b. \tag{B3}$$

The deceleration is largest at $s = 0$, and since we are looking for a critical bed slope for which the flow will separate, this value is used for estimating the deceleration:

$$\frac{d\tilde{u}_a}{ds} \approx -\frac{i_b}{d_0}\tilde{u}_{a,0}. \tag{B4}$$

This deceleration will be related to a critical bed slope, $i_{b,c}$. Using the Von Karman momentum integral equation (equation (B1)), we define a critical deceleration, that is not explicitly resolved, but which is assumed to be a function of the bed shear stress and the (local) boundary layer characteristics:

$$\left.\frac{d\tilde{u}_a}{ds}\right|_{\text{crit}} = \phi_c(\tau_b, \theta, \delta^*), \tag{B5}$$

where ϕ_c is a critical value for the deceleration. Then, a critical bed slope for which the flow separates for a lateral uniform flow is given by

$$i_{b,c} = -\phi_c \frac{d_0}{\tilde{u}_{a,0}}. \tag{B6}$$

The same can be done for a flow that is nonuniform in lateral direction. In this case, we have to take into account that due to the conservation of potential vorticity, there is an additional acceleration at the high-velocity side of the velocity profile ($n = n_U = \frac{1}{2}B$) sketched in Figure B1. An expression for the velocity at the high-velocity side of the profile is given by

$$\tilde{u}_{nU}(s) = \tilde{u_a}(s) + \frac{1}{2}\Delta\tilde{u}(s). \tag{B7}$$

In this expression, the velocity difference $\Delta\tilde{u}$ is given by

$$\Delta\tilde{u}(s) = \tilde{\omega}(s)B, \tag{B8}$$

where $\tilde{\omega}(s)$ is

$$\tilde{\omega}(s) = \tilde{\omega}_0 \frac{d(s)}{d_0}. \tag{B9}$$

The derivative of the velocity at the high-velocity side can now be evaluated:

$$\frac{d\tilde{u}_{nU}}{ds} = -\frac{\tilde{u}_{a,0}d_0}{d(s)^2}i_b + \frac{1}{2}\frac{\Delta\tilde{u}_0}{d_0}i_b. \tag{B10}$$

Again, the value at $s = 0$ is considered, and following the same line of reasoning as with the laterally uniform flow, the critical bed slope for the laterally nonuniform flow ($i^*_{b,c}$) is expressed as

$$i^*_{b,c} = \phi_c \left(\frac{\Delta\tilde{u}_0}{2d_0} - \frac{\tilde{u}_{a,0}}{d_0}\right)^{-1}. \tag{B11}$$

The critical bed slope for which the flow is expected to separate for a laterally uniform flow can now be related to the critical bed slope for which flow separation is expected to occur for a laterally nonuniform flow by dividing equation (B11) by equation (B6). We do make the remark that, since we have not explicitly computed ϕ_c, we do have to introduce some (unknown) proportionality constant α. This analysis is mainly performed to demonstrate that lateral nonuniformity in the flow may steepen the slope for which vertical flow separation would be expected, which is finally expressed as

$$\frac{i^*_{b,c}}{i_{b,c}} \propto \left(1 - \alpha\frac{\Delta\tilde{u}_0}{2\tilde{u}_{a,0}}\right)^{-1}. \tag{B12}$$

B2. Derivation of the Solution for the Idealized Model Application

This section shows the derivation of equation (16) in section 4.2 for an idealized bathymetry: a linearly sloping bed (equation (14)). We prescribe a jet-type velocity profile at the inflow boundary $s = 0$:

$$u(0,n) = u_c \exp\left[-\frac{n^2}{2\sigma^2}\right], \tag{B13}$$

with the parameters defined in section 4.2. From this expression, the vorticity at the inflow boundary is simply derived:

$$\omega(0,n) = \frac{y}{\sigma^2} u_c \exp\left[-\frac{n^2}{2\sigma^2}\right]. \tag{B14}$$

Equation (10) now gives the vorticity at any location in the domain:

$$\omega(s,n) = \gamma \frac{y}{\sigma^2} u_c \exp\left[-\frac{n^2}{2\sigma^2}\right], \tag{B15}$$

where $\gamma = d(s,n)/d(0,n)$ is the ratio of the depth at s with the depth at the inflow boundary. The velocity is obtained by integration of the vorticity:

$$u(s,n) = \gamma u_c \exp\left[-\frac{n^2}{2\sigma^2}\right] + C, \tag{B16}$$

where C is an integration constant that is solved by applying mass conservation over a lateral transect. We apply the following integration rule:

$$\int_{-\infty}^{\infty} \exp\left[-\frac{n^2}{2\sigma^2}\right] dn = \sqrt{2\pi}\sigma. \tag{B17}$$

Although we are not integrating over an infinite domain, we have chosen the velocity profile such that the lateral derivative of the velocity at the sides is approximately zero, making the error very small. Then the analytical expression for the streamwise velocity is given by

$$u(s,n) = \gamma u_c \cdot \exp\left[-\frac{n^2}{2\sigma^2}\right] + \sqrt{2\pi} \cdot u_c \sigma(\gamma^{-1} - \gamma) B^{-1}. \tag{B18}$$

Notation

- $\boldsymbol{B}$ Domain width (m)
- $\boldsymbol{c_f}$ Dimensionless bed friction coefficient (–)
- $\boldsymbol{C}$ Integration constant (m/s)
- $\boldsymbol{C_i}$ Cross section, $i = 0,1$
- $\boldsymbol{d}$ Water depth (m)
- $\boldsymbol{D}$ Width of a single pillar of the barrier (m)
- $\boldsymbol{D_p}$ Heart-to-heart distance between pillars (m)
- $\boldsymbol{f}$ Coriolis parameter (rad/s)
- $\boldsymbol{g}$ Gravitational constant (m/s^2)
- $\boldsymbol{\Delta h}$ Water level difference between inside and outside the barrier (m)
- $\boldsymbol{H}$ Vertical length scale (m)
- $\boldsymbol{i_b}$ Bed slope (–)
- $\boldsymbol{i_{b,c}}$ Critical bed slope for flow separation laterally uniform case (–)
- $\boldsymbol{i^*_{b,c}}$ Critical bed slope for flow separation laterally nonuniform case (–)
- $\boldsymbol{K_W}$ Inlet Strouhal number (–)
- $\boldsymbol{l_m}$ Mixing length (m)
- $\boldsymbol{L_s}, \boldsymbol{L_n}$ Length scale (m)
- $\boldsymbol{n_U}, \boldsymbol{n_L}$ Upper and lower lateral boundary of the domain (m)
- $\mathbf{R}_i$ Sailed transect at Roompot inlet, $i = 1, \ldots, 4$
- $\boldsymbol{s}, \boldsymbol{n}$ Coordinates according to local coordinate system (m)
- $\boldsymbol{\Delta s}, \boldsymbol{\Delta n}$ Grid size in s, n direction (m)
- $\boldsymbol{S}$ Grid solidity (–)
- $\mathbf{S}_i$ Sailed transect at Schaar inlet, $i = 1,2,3$; model transect
- $\boldsymbol{S_{sc}}, \boldsymbol{N_{sc}}$ Scaled streamwise coordinate, scaled transverse coordinate (–)
- $\boldsymbol{t}$ Time (s)

T Tidal period; time scale (s)
ΔT Grid size in temporal direction (s)
T_i Stage in the tidal cycle, i = 1,2,3 (s)
u_0 Streamwise velocity at inflow boundary (depth-averaged) (m/s)
$\bar{\mathbf{u}}$ Depth-averaged velocity vector (m/s)
$\bar{\mathbf{u}}_\perp$ Depth-averaged velocity vector rotated 90° (m/s)
Δu Observed depth-averaged, streamwise velocity difference over a cross section (m/s)
u_a Observed depth-averaged, cross-sectionally averaged, streamwise velocity (m/s)
u_c Magnitude of the centerline velocity of the jet at s = 0 (m/s)
$\overline{u_n}, u_n$ Depth-averaged velocity in n direction (m/s)
$\overline{u_s}, u_s$ Depth-averaged velocity in s direction (m/s)
$\tilde{u}$ Free-stream velocity (m/s)
$\Delta\tilde{u}$ Free-stream velocity difference over cross section (m/s)
$\tilde{u}_a$ Free-stream cross-sectionally averaged velocity (m/s)
U, V Scaled velocity; horizontal velocity scales (–); (m/s)
U_m Maximum cross-sectionally averaged tidal velocity (m/s)
W Inlet width (m)
X, Y Coordinates according to Dutch national RD-coordinate system (m)
z Vertical coordinate (m)
α Parameter relating critical pressure gradients (–)
γ Relative depth increase (–)
δ Mixing layer width (m)
δ^* Displacement thickness (m)
θ Momentum thickness (m)
ν_t Turbulent viscosity (m^2/s)
σ Measure of the width of the jet (–)
ρ Density of water (kg/m^3)
$\bar{\tau}_b$ Bed shear stress (N/m^2)
$\bar{\bar{\tau}}_t$ Depth-averaged horizontal turbulence shear stress tensor (N/m^2)
ϕ Latitude (°)
ϕ_c Critical deceleration for flow separation (m/s^2)
$\tilde{\omega}$ Free-stream vertical vorticity (1/s)
ω_0 Depth-averaged vertical vorticity at inflow boundary (1/s)
ω_e Angular frequency of Earth's rotation (rad/s)
$\overline{\omega_z}, \omega$ Depth-averaged vertical vorticity (1/s)
Ω Scaled vorticity (–)

Acknowledgments
The Dutch Ministry of Public Works, Rijkswaterstaat, is gratefully acknowledged for funding this research and for collecting and providing bathymetric and velocity data. All data used in this study is publicly available through Rijkswaterstaat. We thank three anonymous reviewers for their comments and suggestions that have helped improve this paper.

References

Babarutsi, S., Ganoulis, J., & Chu, V. (1989). Experimental investigation of shallow recirculating flows. *Journal of Hydraulic Engineering*, *115*(7), 906–924.
Balachandar, R., Kells, J., & Thiessen, R. (2000). The effect of tailwater depth on the dynamics of local scour. *Canadian Journal of Civil Engineering*, *27*(1), 138–150. https://doi.org/10.1139/l99-061
Besio, G., Stocchino, A., Angiolani, S., & Brocchini, M. (2012). Transversal and longitudinal mixing in compound channels. *Water Resources Research*, *48*, W12517. https://doi.org/10.1029/2012WR012316
Bey, A., Faruque, M., & Balachandar, R. (2007). Two-dimensional scour hole problem: Role of fluid structures. *Journal of Hydraulic Engineering*, *133*(4), 414–430. https://doi.org/10.1061/(ASCE)0733-9429(2007)133:4(414)
Blanckaert, K. (2010). Topographic steering, flow recirculation, velocity redistribution, and bed topography in sharp meander bends. *Water Resources Research*, *46*, W09506. https://doi.org/10.1029/2009WR008303
Breusers, H., Nicollet, G., & Shen, H. (1977). Local scour around cylindrical piers. *Journal of Hydraulic Research*, *15*(3), 211–252. https://doi.org/10.1080/00221687709499645
Brocchini, M. (2013). Bore-generated macrovortices on erodible beds. *Journal of Fluid Mechanics*, *734*, 486–508. https://doi.org/10.1017/jfm.2013.489
Bryant, D., Whilden, K., Socolofsky, S., & Chang, K. (2012). Formation of tidal starting-jet vortices through idealized barotropic inlets with finite length. *Environmental Fluid Mechanics*, *12*(4), 301–319. https://doi.org/10.1007/s10652-012-9237-4
Buschman, F. (2017). Determining flow velocity near the bed in a scour hole using ADCP observations. Netherlands Centre for River studies: Book of abstracts NCR days 2017 (pp. 36-37).
Chang, P. (1970). *Separation of flow* (1st ed.). New York: Pergamon Press.
Cohen, C. (2012). Shallow-water plane and tidal jets. Thesis, doctor of philosophy, University of Otago. Retrieved from http://hdl.handle.net/10523/2493

D'Agostino, V., & Ferro, V. (2004). Scour on alluvial bed downstream of grade-control structures. *Journal of Hydraulic Engineering*, *130*(1), 24–37. https://doi.org/10.1061/(ASCE)0733-9429(2004)130:1(24)
Dargahi, B. (1990). Controlling mechanism of local scouring. *Journal of Hydraulic Engineering*, *116*(10), 1197–1214.
Dargahi, B. (2003). Scour development downstream of a spillway. *Journal of Hydraulic Research*, *41*(4), 417–426. https://doi.org/10.1080/00221680309499986
Dracos, T., Giger, M., & Jirka, G. (1992). Plane turbulent jets in a bounded fluid layer. *Journal of Fluid Mechanics*, *241*, 587–614. https://doi.org/10.1017/S0022112092002167
Falcini, F., & Jerolmack, D. J. (2010). A potential vorticity theory for the formation of elongate channels in river deltas and lakes. *Journal of Geophysical Research*, *115*, F04038. https://doi.org/10.1029/2010JF001802
Guan, D., Melville, B., & Friedrich, H. (2014). Flow patterns and turbulence structures in a scour hole downstream of a submerged weir. *Journal of Hydraulic Engineering*, *140*(1), 68–76. https://doi.org/10.1061/(Asce)Hy.1943-7900.0000803
Hench, J., Blanton, B., & Luettich, R. (2002). Lateral dynamic analysis and classification of barotropic tidal inlets. *Continental Shelf Research*, *22*(18–19), 2615–2631. https://doi.org/10.1016/S0278-4343(02)00117-6
Hoffmans, G., & Booij, R. (1993). Two-dimensional mathematical modelling of local-scour holes. *Journal of Hydraulic Research*, *31*(5), 615–634. https://doi.org/10.1080/00221689309498775
Hoffmans, G., & Pilarczyk, K. (1995). Local scour downstream of hydraulic structures. *Journal of Hydraulic Engineering*, *121*(4), 326–340.
Hoffmans, G., & Verheij, H. (1997). *Scour manual*. The Netherlands: A.A. Balkema Publishers Rotterdam.
Hogg, A., Huppert, H., & Dade, W. (1997). Erosion by planar turbulent wall jets. *Journal of Fluid Mechanics*, *338*, 317–340.
Jirka, G. (2001). Large scale flow structures and mixing processes in shallow flows. *Journal of Hydraulic Research*, *39*(6), 567–573. https://doi.org/10.1080/00221686.2001.9628285
Jirka, G. H., & Seol, D. G. (2010). Dynamics of isolated vortices in shallow flows. *Journal of Hydro-Environment Research*, *4*(2), 65–73. https://doi.org/10.1016/j.jher.2010.04.011
Kwoll, E., Venditti, J. G., Bradley, R. W., & Winter, C. (2016). Flow structure and resistance over subaquaeous high- and low-angle dunes. *Journal of Geophysical Research: Earth Surface*, *121*, 545–564. https://doi.org/10.1002/2015JF003637
Lenzi, M., Marion, A., Comiti, F., & Gaudio, R. (2002). Local scouring in low and high gradient streams at bed sills. *Journal of Hydraulic Research*, *40*(6), 731–739. https://doi.org/10.1080/00221680209499919
Manes, C., & Brocchini, M. (2015). Local scour around structures and the phenomenology of turbulence. *Journal of Fluid Mechanics*, *779*, 309–324. https://doi.org/10.1017/jfm.2015.389
Melville, B. (1995). Bridge abutment scour in compound channels. *Journal of Hydraulic Engineering*, *121*(12), 863–868. https://doi.org/10.1061/(ASCE)0733-9429(1995)121:12(863)
Nicolau Del Roure, F., Socolofsky, S., & Chang, K. (2009). Structure and evolution of tidal starting jet vortices at idealized barotropic inlets. *Journal of Geophysical Research*, *114*, C05024. https://doi.org/10.1029/2008JC004997
Poulin, F., & Flierl, G. (2005). The influence of topography on the stability of jets. *Journal of Physical Oceanography*, *35*(5), 811–825. https://doi.org/10.1175/JPO2719.1
Rajkumar, V., & Dey, S. (2008). Kinematics of horseshoe vortex development in an evolving scour hole at a square cylinder. *Journal of Hydraulic Research*, *46*(2), 247–264. https://doi.org/10.1080/00221686.2008.9521859
Rodi, W. (1980). *Turbulence models and their application in hydraulics*. Karlsruhe: IAHR.
Schnauder, I., & Sukhodolov, A. (2012). Flow in a tightly curving meander bend: Effects of seasonal changes in aquatic macrophyte cover. *Earth Surface Processes and Landforms*, *37*(11), 1142–1157. https://doi.org/10.1002/esp.3234
Schreutelkamp, F., & Strang van Hees, G. (2001). Benaderingsformules voor de transformatie tussen RD- en WGS84-kaartcoördinaten. *Geodesia*, *2*, 64–69.
Shiono, K., & Knight, D. (1991). Turbulent open-channel flows with variable depth across the channel. *Journal of Fluid Mechanics*, *222*(-1), 617. https://doi.org/10.1017/S0022112091001246
Signell, R., & Geyer, W. (1991). Transient eddy formation around headlands. *Journal of Geophysical Research*, *96*(NO. C2), 2561–2575.
Simpson, R. L. (1989). Turbulent boundary-layer separation. *Annual Review of Fluid Mechanics*, *21*, 205–234.
Stocchino, A., Besio, G., Angiolani, S., & Brocchini, M. (2011). Lagrangian mixing in straight compound channels. *Journal of Fluid Mechanics*, *675*, 168–198. https://doi.org/10.1017/S0022112011000127
Talstra, H. (2011). Large-scale turbulence structures in shallow separating flows. Thesis, doctor of philosophy, Delft University of Technology.
Termini, D., & Sammartano, V. (2012). Morphodynamic processes downstream of man-made structural interventions: Experimental investigation of the role of turbulent flow structures in the prediction of scour downstream of a rigid bed. *Physics and Chemistry of the Earth*, *49*, 18–31. https://doi.org/10.1016/j.pce.2011.12.006
Turner, J. S. (1986). Turbulent entrainment: the development of the entrainment assumption, and its application to geophysical flows. *Journal of Fluid Mechanics*, *173*, 431–471. https://doi.org/10.1017/S0022112086001222
Uijttewaal, W., & Jirka, G. (2003). Grid turbulence in shallow flows. *Journal of Fluid Mechanics*, *489*, 325–344. https://doi.org/10.1017/S0022112003005020
Valle-Levinson, A., & Guo, X. (2009). Asymmetries in tidal flow over a Seto Inland Sea scour pit. *Journal of Marine Research*, *67*(5), 619–635. https://doi.org/10.1357/002224009791218850
van Prooijen, B., Battjes, J., & Uijttewaal, W. (2005). Momentum exchange in straight uniform compound channel flow. *Journal of Hydraulic Engineering*, *131*(March), 175–183. https://doi.org/10.1061/(ASCE)0733-9429(2005)131:3(175)
van Prooijen, B., & Uijttewaal, W. (2002). A linear approach for the evolution of coherent structures in shallow mixing layers. *Physics of Fluids*, *14*(12), 4105–4114. https://doi.org/10.1063/1.1514660
van Velzen, G., Raaijmakers, T., & Hoffmans, G. (2015). Scour development around the Eastern Scheldt storm surge barrier-field measurements and model predictions, Proceedings of the 7th International Conference on Scour and Erosion Perth Australia (pp. 693–704).
Vermeulen, B., Hoitink, A., & Labeur, R. (2015). Flow structure caused by a local cross-sectional area increase and curvature in a sharp river bend. *Journal of Geophysical Research: Earth Surface*, *120*, 1771–1783. https://doi.org/10.1002/2014JF003334
Wan, Z., Huang, S., Sun, Z., & You, Z. (2015). Stability of jets in a shallow water layer. *International Journal of Numerical Methods for Heat & Fluid Flow*, *25*(2), 358–374. https://doi.org/10.1108/HFF-04-2013-0137
Wells, M., & van Heijst, G. (2003). A model of tidal flushing of an estuary by dipole formation. *Dynamics of Atmospheres and Oceans*, *37*(3), 223–244. https://doi.org/10.1016/j.dynatmoce.2003.08.002
Wolanski, E., Drew, E., Abel, K., & O'Brien, J. (1988). Tidal jets, nutrient upwelling and their influence on the productivity of the alga Halimeda in the Ribbon Reefs, Great Barrier Reef, Estuarine. *Coastal and Shelf Science*, *26*(2), 169–201. https://doi.org/10.1016/0272-7714(88)90049-2